LRP 683/00 October 2000

Invited and contributed Papers
presented at the

21st Symposium on Fusion Technology
S O F T

September 11-15, 2000
Madrid, Spain

ISSN 0458-5895

LIST OF CONTENTS

30 kV/10mA SOLID STATE ANODE MODULATOR FOR GYROTRON PLASMA HEATING, DESIGN ISSUES AND RESULTS.

D. Fasel (CRPP), C. Lucía (JEMA), D. Ganuza (JEMA), I. Doyharzabal (JEMA)
JEMA, 20160 Lasarte-Oria, Spain
CRPP, Association EURATOM-Confédération Suisse, PPH, CH-1015 Lausanne, Switzerland

ABSTRACT

Three 30kV/10mA solid state pulsed modulators have been delivered to the CRPP in Lausanne, by the company JEMA. Each modulator supplies the anode grid of a triode type gyrotron, used for heating purpose at the third harmonic in the TCV Tokamak.
The main parameters of the final design are the following: the use of solid state technology, a floating output referred to the -80kV of the gyrotron cathode potential, an output voltage range of -5kV to 30kV, 1 kHz square and sinusoidal modulation, fast switching off to -5kV (10 µsec) and pulsed operation (duty cycle of 1%).
The most important difficulty arising in the project concerns the discharge of the approximately 200 pF stray capacitance, in parallel with the 3 MOhm equivalent resistor load of the gyrotron. Another disturbing element is the stray capacitance between anode and ground, which produces a non negligible current flowing through the modulator when the -80kV of the cathode are applied and removed (dV/dt effect).
After studying and testing a solution based on regulated Mosfet transistors in series, a more stable alternative has been adopted. The final topology consists of a rectifier fed from an insulated 230V input, a chopper, two inverter steps (for +30kV and -5kV) supplying two diode rectifiers bridges through HV transformers with two switches which commute the load to the positive or negative voltage, connected in series.
The voltage regulation is carried out on the low voltage side, by means of the chopper. This system provides a non-linear response. While the rising voltage at the HV output is fast, the falling curve is determined by the RC value of the load. There is a possibility of decreasing the time constant by connecting an additional resistive load in parallel, but limited by the maximum input power available of 3kVA.
In order to achieve square modulations of 5kV at 1kHz, and considering that the time constant is not lower than 500µs, special attention has been paid to the regulation principle, based on the use of a feed-forward table, which results in a significant improvement of the total response time. In combination with an open loop algorithm, a PI controller ensures the stability requirements: ± 0.5 % of the nominal output voltage.
This article presents the most significant aspects of the design, with special emphasis on the control principle. The minimisation of the voltage overshoot during the modulation and the transmission of the analog insulated measurements via serial optic links are also described. The final results will be presented in the context of normal operation, supplying a triode gyrotron.

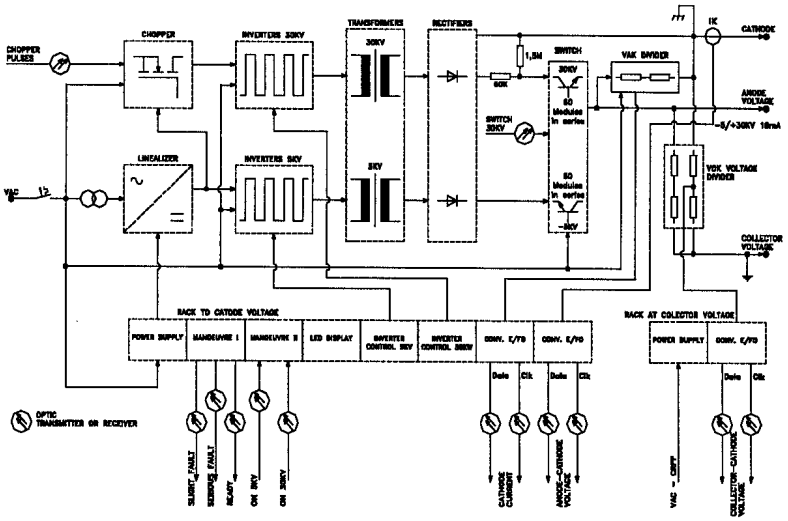

Figure1: General Diagram

1. BACKGROUND

Before describing the solution proposed by JEMA to supply the anode of three gyrotrons used for heating purposes in TCV (CRPP), we will enounce the most relevant points of the specification. 30kV / 10mA insulated power supplies are required. One of the power supply terminals is connected to the cathode of the gyrotron, at a -80kV potential referred to the ground. A square or a sinus wave modulation of 5kV peak to peak at a max frequency of 10 kHz is asked by specifications. The input power drawn from the mains is limited to 3kVA. For gyrotron protection purpose, a fast blocking behaviour (in the range of 10 µsec) to –5kV must be implemented.

Additional requirements concern the accuracy and the large bandwidth of voltages measurements: anode to cathode voltage (Vak) and collector to cathode voltage (Vck).

Upon these requirements, JEMA has proposed an initial solution based on solid state technology. The main subassemblies are:

- A linealizer at the input, ensuring a stabilized DC voltage without waveform distortion on the input current.
- Two inverters coupled to high voltage transformers in order to obtain the non-stabilised 30kV and -5kV DC output voltages.
- Two high voltage switches, comprising each 60 modules in series, based on Mosfet.

In the initial approach, the high voltage switches worked as voltage regulators. Due to stability and reliability problems during the testing phase, an alternative solution has been studied and implemented.

In the final solution, the high voltage switches have been released of the regulation function and focused only on the protection requirements. The regulation has been implemented in the low voltage DC side, by means of a chopper, inserted between the linealizer and the input of the 30kV inverter. This solution is much more reliable than the previous one.
As the high voltage switches can not be used anymore for regulation purpose, an resistive load has been added in parallel at the output of the power supply, in order to discharge the stray capacitance found between anode and cathode, and so to fulfil the dynamic requirements.
The Figure 1 presents the schematic of the power supply which has been commissioned at the CRPP. A description of the most highlighting point concerning the design and the regulation principle is presented in the following sections.

2. LINEALIZER AND CHOPPER

A standard 3kVA linealizer from JEMA has been used. This module provides a stabilized voltage of 350Volt at its output. The input current is sinusoidal and the power factor is practically equal to 1.

The chopper is implemented by means of a Mosfet module. The chopping pulses, generated at a frequency of 40kHz in the control system on the low voltage side, are transmitted directly to the Mosfet driver through a fiber optic link.

3. INVERTERS AND HV RECTIFIERS.

Two square wave inverters have been implemented in order to obtain the required 30kV and -5kV blocking voltage. We will discuss the 30kV inverter, which involves more insulation and design issues.

Four inverter modules of H bridge type have been implemented by means of Mosfet transistors. The commutation frequency is 20kHz. The inverters start up in ramp and work at the maximum modulation rate, which produces a lower ripple voltage in the rectified waveform.

Each inverter is connected to the primary of a high voltage transformer wound on a ferrite core. These transformers are the most critical part of the design because they have to meet two contradictories requirements:

- The minimization of the whole assembly size in order to decrease the stray inductance and capacitance values.
- The observation of the insulation distances.

The support of the cores, made of Teflon, ensures a 30kV insulation between the primary and the secondary windings, which consist of 400 turns distributed on 4 layers. The insulation between layers is realized by thin foils of Teflon. Special care has been taken in the winding technique, in order to optimize the insulation distances. Each secondary winding has been dried and sailed with enamel, avoiding insulation failures due to condensation.

A high voltage diodes bridge is connected to the secondary winding terminals of each transformer. Each high voltage diodes rectifier comprises 25 diodes in series, mounted on a printed circuit board, including the parallel resistors to ensure a good voltage equalization.

4. HIGH VOLTAGE SWITCHES

The high voltage switches, formed by 60 Mosfet modules in series are described hereafter.

Each switching 1000V Mosfet transistor is controlled by the same reference, distributed to each module through an isolated cable carrying a current signal. This reference is transmitted to the modules through a hall effect transducer, part of each module, ensuring an isolated transmission.

The supply energy, required by the electronics of each module, is drawn through a 50Hz current transformer, using the same principle as described above for the module reference.

In order to obtain a suitable dynamic and static behaviour, as for protection purposes, each module incorporates a RC network and a 575 Volt varistor in parallel with its output terminals.

5. CONTROL AND REGULATION

The control system is implemented in a 3U 19" standard rack, referred to ground. Due to this requirement, all the signals and measurements are transmitted by means of silica fibers optic.

The control logic has been implemented in a 128 Macrocell PLD.

The voltage regulation and the communication interface with the CRPP control system have been implemented in the W4050 board from JEMA. On this multiple-use board, a PIC16V77 microcontroller is dedicated to the communication with the CRPP interface (via RS232) and

to generate an internal voltage reference, including few parameters allowing to change the pulse timing, the voltage level and the modulation configuration: type, frequency, amplitude and duration.
The regulation has been implemented on a FLEX10K20 FPGA (Fast Programmable Gate Array). Two main aspects have to be taken in consideration concerning the regulation:

- The transfer function is intrinsically non-linear. The power supply is able to rise the Vak voltage, but not to ramp it down without closing the blocking switch. If the 30kV power supply is disconnected, the output voltage falls exponentially, with an RC characteristic determined by the stray anode-cathode capacitance (Cak = 150nF), the Rload (≈3Mohm) and the additional load in parallel. The time constant value measured is 600 µsec.
- The load (the anode grid of the gyrotron) can be supposed to have a repetitive behaviour. This point is very important because it enables the use of feedforward algorithms, based on the direct calculation of the instantaneous modulation rate, depending on the voltage reference and the transfer function of the system.

Instead of determining the exact transfer function, a feedforward characteristic has been evaluated in the following way. A look-up table has been created for each power supply, following these steps:

- Few pulses have been made, using different modulation duty cycles to drive the chopper Mosfet, then, for each pulses, the DC output voltage has been acquired.
- Based on the results obtained, 12 couples of points (modulation rate, output voltage) have been memorized in order to create a feed-forward look-up table using a linear interpolation.

Additionally to the feedforward term, a PI closed loop controller works in parallel. This PI controller provides the required accuracy, while the feed-forward controller improves the time response and minimizes voltage overshoots.

Another important issue concerns the square modulation in the most critical conditions (1kHz, 5kVpp). The 600 µsec time constant limits the max modulation frequency. Once again the solution to this problem has been found from the observation of the feed-forward features. Seen that the normal modulation conditions consider a flat top at 25kV, the system calculates the time value during which the duty cycle of the chopper has to be kept to 0 in order to decrease faster the voltage to the value "Vflat_top – Vmodulation". For example, considering a modulation between 25kV and 20kV, and a time constant of 600 µsec, the off time value is:

$$t_o = -\tau \cdot \ln\left\{\frac{V_{inf}}{Vsup}\right\} \rightarrow t_o = 134 \cdot \mu s \qquad (1)$$

Where V_{sup} (25000 Volts) and V_{inf} (20000 Volts) are the upper and lower voltages of the square modulation, τ (600µs) is the time constant of the output load and t_o is the time while the duty cycle of the chopper has to be kept to 0 (in order to decrease the voltage from V_{sup} to V_{inf}).

The obtained results with this principle are represented in Figure 2.

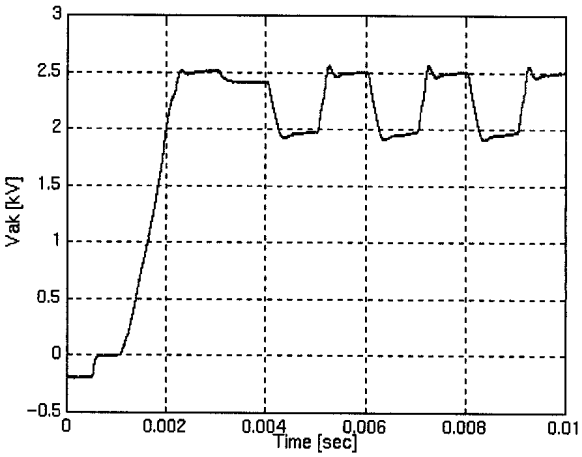

Figure 2: Modulation at 5kV, 500Hz

6. MEASUREMENTS

Three analog measurements are required: Vak and Vck voltages, and the anode current (Ia). The voltage measurements must respect an accuracy value of ±0.5% and a bandwidth of 1MHz. Due to the difficulties to find on the market a complete system, able to transmit optically these measurements and able to achieve the conditions listed above, JEMA has developed its own optical transmission link comprising: one transmitter unit, one receiver unit and two fibers optic link. Both transmitter and receiver are housed in standard 10U sub-modules for 19"racks.

The transmitter module is made of an analog signal input connector, a matching impedance, a 10 bit ADC converter, a PLD which implements the serial transmission protocol and two fibers optic transmitters: one for the Data link and the other one for the CLK link, used to synchronize the transmitter and the receiver.

The receiver module is composed of two fibers optic receivers, a PLD, a DAC converter and an analog output signal connector.

Both modules include a back panel connector with 12 of its terminals (10 in the receiver) connected to the PLD. This feature allows a digital transmission of the analog signals through the back plane. Thus, the control system can manage digitally the measurements, which improves the noise rejection is by eliminating redundant digital to analog translations.

Voltage dividers are used for the Vak and Vck measurements. The anode current measurement is carried out by means of a hall effect current transducer.

7. FINAL RESULTS

The main conclusion from this work is that, anode modulators, which have been traditionally based on vacuum tubes, can be successfully implemented with a more relevant solid state technology.

The three power supplies have been commissioned on the CRPP site and actually two units have been successfully used, working with gyrotron load. The third one will be used during the commissioning of the last gyrotron, in September. Following are presented some relevant results (Figures 3, 4 and 5).

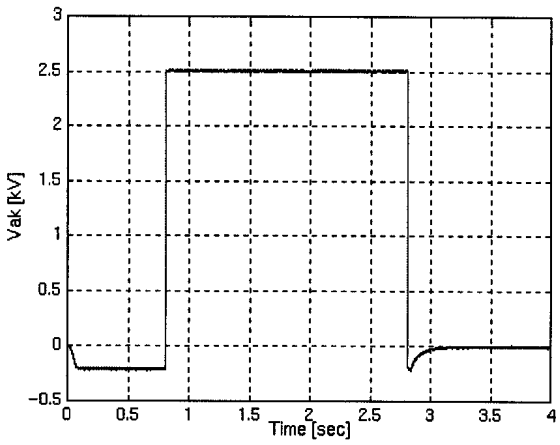

Figure 3: 2 seconds pulse at 25kV.

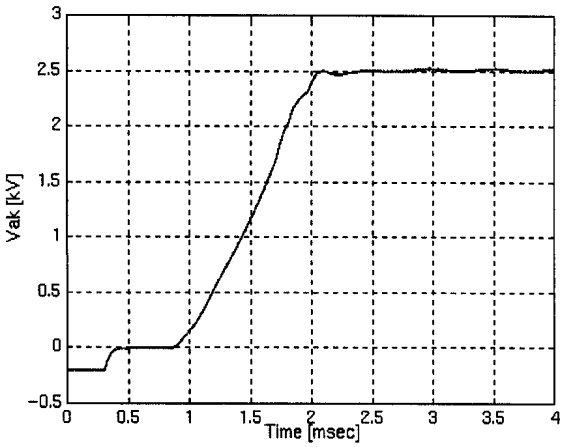

Figure 4: zoom of the voltage ramp-up characteristic.

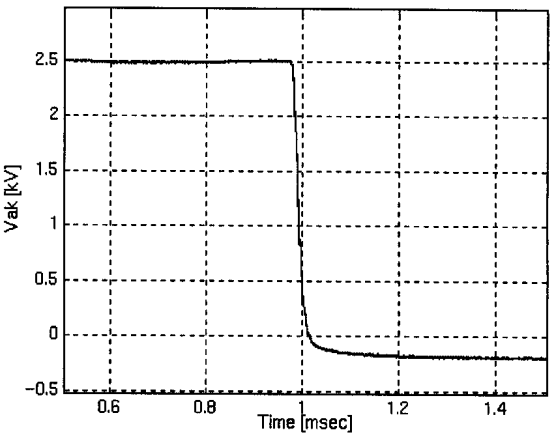

Figure 5: zoom of the voltage falling characteristic.

Evolution not Revolution in the TCV Tokamak Control and Acquisition System

B.P. Duval, X. Llobet, P.F. Isoz, J.B. Lister, B. Marletaz, Ph. Marmillod and J-M. Moret

Centre de Recherches en Physique des Plasmas- EPFL

PPB120, EPFL, 1015 Lausanne, Switzerland

Abstract

The original TCV control system was designed in the late 1980s to be inherently network based in that all control operations were performed from X-windows terminals and the control computers were networked. Using VMS-VAX technology, the acquisition system (CAMAC) and control system (BITBUS) were connected to controllers situated in the machine bus of these machines that were linked homogeneously by the VMS "cluster" technology.

Although the computing power and network bandwidth have improved considerably over the last years, the data acquired has risen from ~10Mbyte to ~200Mbyte per plasma discharge from increasingly numerous and complex diagnostic and acquisition systems. The goal over this period has thus been to evolve the control and acquisition systems to embrace new technologies whilst retaining the remote and automatic features. This paper describes changes in both the hardware and software which leave TCV in a state whose structure is coherent with its origins yet includes many new

components. To control this increased complexity, a very general and symmetric software paradigm was developed based on an efficient matrix capable interpreter that is part of the MdsPlus package. This Tree Data Interface (TDI) package has many of the Matlab/IDL capabilities together with the explicit capability of calling dynamic libraries directly. There is also a TDI TCP/IP server for a remote client to call these functions and obtain a reply. With the recent port of MdsPlus to many Unix flavours, WinXX and VMS where the different binary formats are transparently translated, communication between most all computers at TCV can be performed over the same interface. By now writing all the CAMAC, BITBUS and database handling routines in this language, all the TCV functionality is symmetrically available across all platforms. Client interfaces from C, Fortran, MatLab, IDL, Java, etc. are available for execution of TDI functions on local and remote machines. By ensuring that new control or computing hardware in supplied with this interface, it is possible to not only control all TCV functions from our central computers, but to further evolve the system by exporting some or all control to another computer with different architecture whilst retaining the same TDI routines.

1 Introduction

In the ~10 years that the TCV tokamak has been in operation, there has been a vast change in both the user's needs for system control and acquisition, and in the number of commercial systems available. This situation has been further complicated with the purchase of "State of the Art" diagnostic systems equipped with an amazing variety of hardware and software systems. Although TCV has a relatively limited staff available for maintaining these systems, (we tend to preferentially hire physicists), the complexity of even standard diagnostic systems has also increased many-fold. From

the outset, it was decided that ALL control and diagnostic systems were to be operable remotely which, although complicating the initial system installation, permitted the subsystems to operate with little manual assistance liberating the personnel to spend more time in the analysis of the experimental data.

Together, these requirements create a tough challenge in the design and maintenance of a control and acquisition system. New technology must be incorporated into an existing and running system maintaining backward compatibility and the steadily increasing quantity of data must be quickly available for online and post experiment analysis. The environment in which this is performed must retain the possibility of future expansion whilst the dedicated personnel requirements are not allowed to increase.

In the rest of this paper, we shall discuss first the control and then the acquisition, storage and data delivery systems as they have evolved while highlighting the manner in which the above constraints were resolved.

2 TCV Control

This section describes the hardware and software, which is used to control the machine and diagnostic systems on TCV including the discharge preparation and real-time sequencing. The control of the plasma and plasma shaping feedback systems is not described here although it is also accessed by the same hardware and details may be found in [1] and the included references.

The BitBus protocol was originally chosen as the TCV control bus. Initially the controllers were housed in a VAX based Q-bus backplane with software from DEC. This system provides for some pseudo-multitasking remote tasks including the RAC-

task, which has standard I/O commands and communication functions. Over the years, a large range of electronic cards (PIO, RS232, ADC, DAC, GPIB, TIMER [2]) have been developed within this bus structure which has benefited from technological developments such as PAL and FPGA electronics to improve the available functionality. By providing a 1MHz synchronous bus in the BitBus cabling, 1us timing resolution is available across the whole machine. Most of these cards can be readily modified to provide further functionality eg: a pair of timer cards have been used to synthesise a Video Genlock signal for the TCV CCD cameras, a DAC card has been programmed to provide a multi-channel programmable signal generator etc.

Although BitBus is nowadays considered out of date, it still performs adequately and it is not foreseen to change the installed systems within the lifetime of TCV.

We chose to replace the BitBus controllers with CAMAC based controllers from Hytec [3], which are controlled from TCP/IP based crate controllers from the same manufacturer who also provide a software library for VMS and UNIX in the form of a shareable library. In this way, the increased number of BitBus nodes, which has increased from ~80 to well over 350 has been split across several BitBus networks.

A large part of the software control of this system was implemented via a live database, [4]. This control system was programmed to execute completion routines when a database value changed eg: changing a value from 0 to 1 would result in a BitBus packet that would open an electrical relay. With database access available within a VMS cluster and a drawing a scripting language provided with the product, machine and diagnostic users wrote graphical interfaces to control and monitor the TCV plant and diagnostics.

As with all software, compatibility problems with later versions of this software have resulted in TCV using an older software version of this database software which unfortunately still runs on VAX hardware. In order to integrate the newer Hytec

BitBus controllers, a client-host TCP/IP based remote BitBus program (REMBB) was written which provides direct BitBus access across the whole TCV VMS cluster. Furthermore, to satisfy the increasing complexity, the software emulated the original DEC API so that all previous software that was designed to operate on a local Q-Bus machine could be transparently used with the new hardware. BitBus crates are now given logical names which are dynamically resolved by a REMBB nameserver so that software and hardware can be developed and debugged in the lab and then installed on the fly into TCV, simply by changing the nameserver entry and sending a reread signal. If a further control bus is installed on TCV, this software indirection could be used to transparently emulate the present functionality. Changes in the sequencing of some of the control parameters are discussed in a later section.

It is important to note that the decision to make TCV security independent of this control bus has been carefully preserved so that the machine security is not endangered by failure of the software.

3 Acquisition and data handling

Originally, BitBus was for control and CAMAC was exclusively used for data acquisition. CAMAC was provided by Kinetic Systems Serial Crate Controllers with a Q-Bus master. With little legacy CAMAC equipment available, modern ADCs from INCAA [5] were purchased for slow (< 20kHz) and fast (1MHz) acquisition. Over the years, the acquisition requirement has risen over tenfold to over 200Mbytes of raw data per plasma discharge (~2sec real time).

In collaboration with the authors at MIT, we use the MdsPlus software suite, which was originally written for VMS, and provides a complete environment for acquiring experimental data and a fast "scope" for quick data display. This is complemented by

a trace based multi dimension database structure in which the TCV data are stored. All the acquisition prepare and store functions are implemented as triggered actions that can execute any program or function. The exploitation of this functionality is described later.

The Q-Bus CAMAC controllers have been replaced in two ways. The serial crate controllers are now connected to TCV by a Jorway SCSI module [6] and the above-mentioned Hytec CAMAC controllers are used for crates containing large amounts of data. The SCSI controller is addressed by a driver that only calls standard SCSI commands, and the Hytec controller is TCP/IP based. Drivers for the limited number of CAMAC modules used on TCV were written to be independent of the CAMAC controller. As above, only a change in the logical name of the CAMAC module is required for the acquisition software to automatically select the correct crate and interface. By splitting the CAMAC modules across several interfaces, data is now acquired in parallel which eases the burden of the increased acquired data on the total acquisition time.

Together with an increase in "standard" ADC trace acquisition requirements, commercial diagnostics with their own acquisition systems, often housed in Wintel computers have become common. Worse still, some systems require particular OS versions to operate correctly so a general OS based network communication solution is not possible.

Over the last years, MIT has ported the MdsPlus software suite to Wintel and most flavours of the UNIX operating system. Together with this, a client-server with remote routine execution was developed (MdsIP) with automatic binary-data translation. Thus, a client on any platform may contact a server on another platform and receive a reply in its own binary format. This approach makes the client relatively simple since the server performs all the computation. MdsIP has been used to

integrate Win98 hosted diagnostics on TCV, required by the 16bit program used by the manufacturer, and WinNT hosted systems are currently being installed. This method solves the requirement of integrating most commercially available equipment but can also be extended to introduce new systems of our own design. In the latest of these systems installed on TCV, a 32 channel 200kHz 16bit PCI card with 64M of onboard memory was developed [7] together with a driver under the Linux operating system which can also run MdsPlus and MdsIP. The acquisition modes available were designed to be similar to our CAMAC modules, with as many as four cards in the same PC. The computing power of a modern PC mean that a single such system has more data memory than was originally available on TCV and that this system can be employed in an autonomous, semi-autonomous or slave mode via MdsIP. In one such system, data from our power supplies will be acquired for each plasma discharge and stored to local hard disk with only a résumé data set permanently stored in our main shot database. If an error is detected, the operator can look at the complete data set remotely and choose to store a larger data set to the main database with a backlog memory limited only by the locally available disk space.

This kind of hardware design opens up new possibilities of remote data acquisition and pre-treatment with cheap widely available PC hardware to our specifications. Often considerably cheaper than a CAMAC based system, TCV is now able to choose acquisition solutions that are readily integratable into our current system from a wide range of hardware and software platforms.

Access to the main database is also provided via the MdsIP interface, which allows shot data to reside on one machine and be accessed by multiple platforms via relatively simple clients. At TCV, where Matlab is popular, an MdsIP client is available that compiles on Wintel, VMS and many UNIX systems (Linux, IBM, Compaq, SUN, Solaris...)

4 Putting it all together

The major change in the TCV control and acquisition systems is the way they are now being symmetrically integrated via a common passerelle. With the incredible increase in raw computing power, the penalty in using semi-interpreted, but numerically rich, computing languages like Matlab and IDL, instead of compiled code, has become negligible. MdsPlus comes with a relatively simple version of these languages named TDI, which is first-time interpreted and where variables are stored together with a descriptor of their dimensions and binary format. It features a very C-like command set and the ability to dynamically call routines in shareable libraries with data in the stack or pointers to the data or a data structure. Suites of functions have been written in this language which can communicate with the live VISTA database, address BitBus nodes, address CAMAC modules, get and put data into the main databases, and connect to other computers via MdsIP. TDI can handle string, vector and Matrix manipulations and can always be enhanced with a home written shareable library routine to perform any other required function. Its C-like scripting functions make it potent for writing complex sequences as required and in efficiently handling large amounts of data. Since TDI is available in all the systems to which MdsPlus has been ported and is mostly royalty free (contact MIT), these routines, once developed, can be freely transferred to other operating systems without translation. Further to this, it is now important to note that the MdsIP interface simply provides the ability to execute one of these TDI functions on a remote computer and obtain the result, be it a string, a constant, a vector or a multi-dimension matrix. Thus, if one of the TCV computer systems can perform a function with a particular piece of hardware or software, then all TCV computers have access to this function by MdsIP. Conversely,

if a TCV computer wishes to distribute some complex calculation, it can connect via MdsIP to a powerful calculator and request this calculation. The calculator itself can obtain further data or parameters from other machines, as required, using another MdsIP connection. Since all MdsPlus actions can be invoked by function calls in the TDI language, maintenance of the acquisition structure often simply implies resolving a bug in one of the text based TDI functions, or the development of a more appropriate function which itself has full access to the TCV plant.

With all of the current control and acquisition available to TDI, and ALL new systems required to provide access through the MdsIP call, TCV can now integrate new devices, harness more computing and storage systems and access all the databases across all the platforms. With MdsIP clients available in Matlab, IDL, JAVA, C, Fortran and even TDI itself, this access is more or less universal.

It is important to note that since MdsIP is of course TCP/IP based that, with the correct precautions as to data and machine access, (passwords, privileges, firewalls, SSH, VPN etc) all this power is inherently, and automatically, available remotely. In a true sense, TCV is operated locally as if it were remote.

5 Conclusions and outlook

Although we hope to have shown that TCV has indeed evolved during its operation whilst maintaining short and long-term compatibility, we also hope to have demonstrated how much it has changed. From a albeit networked VMS cluster with hardware in a Q-bus backplane, TCV now hosts seemingly all the operating systems currently available yet with little extra cost in terms of software complexity or maintenance. It is interesting to note that most of the software components mentioned in this paper were available at the start of TCV operations. What has changed is the

realisation that the concept of a scriptable and interpreted language, which we were already using for data analysis (Matlab), could be applied to all our control and data acquisition requirements with the addition of only minor compiled programming "glue". With the recent addition of implicit network connection and transparent binary data translation, the TDI language satisfies all our requirements and its calculation efficiency can be used to rapidly evaluate functions of raw traces dynamically.

We believe that since it is now accepted that the same ASCII command on our Wintel, VMS or UNIX systems and yields the same reply in native binary format, that the system has even become simpler. The functional position of each hardware and software component is well defined and has been shown to be replaceable with a modern component with the same functionality without causing discontinuities in the plant availability.

We have currently decided to leave VMS for some of the more calculation speedy UNIX systems with little change as seen by the users in their Matlab environment. We are strongly considering the transfer of our main databases from VMS to UNIX filesystems for performance reasons although we may leave the CAMAC and BitBus control on VMS which would then become a client much like the Linux based ADCs described above. It may become necessary to move the BitBus control and CAMAC (both SCSI and TCP/IP) to UNIX directly should we find this more efficient, and the required drivers are already available. The MdsIP interface is being provided with data compression and extra security extensions in order to preserve network bandwidth and integrity in an optional and extensible manner providing remote data access for an increasing number of off-site collaborations.

In all of this, we conclude by noting that each of these steps can be performed independently as and if required by particular or general performance needs at TCV.

References

[1] J.B. Lister, et al., The control of Tokamak Configuration Variable plasmas, Fusion Technology 32 (1997) 321-373.

[2] J.B. Lister, Ph. Marmillod, P.-F. Isoz, B. Marletaz, and I.E. Piacentini, Distributed control of the TCV Tokamak and modular BitBus nodes, Proc. 16th Symp. Fusion Technology, London, U.K., September 3-7, 1990. North-Holland Publishing Company (1991)

[3] Hytec Electronics Ltd, 5 Cradock Road, Reading, Berkshire, RG2 0JT, England Web-site: www.hytec-electronics.co.uk

[4] Vista Control Systems, 176 Central Park Square, Los Alamos, NM 87544, USA. Web-site: www.vista-control.com

[5] INCAA Computers BV, P.O. Box 722, 7300 AS Apeldoorn, The Netherlands Web-site: www.incaacomputers.com

[6] Jorway Corporation, 27 Bond St, Westbury, NY 11590, USA E-mail: info@jorway.com

[7] D-TACQ Solutions Ltd, James Watt Building, Scottish Enterprise Technology Park, East Kilbride, Scotland, G75 0QD Web-site: www.d-tacq.com

Linear and Non-linear Plasma Equilibrium Responses on the JT-60U and TCV Tokamaks

J.B. Lister[1], R. Khayrutdinov[2], D.J.N. Limebeer[5], V. Lukash[3], Y. Nakamura[4], A. Sharma[5], F. Villone[6], J.P. Wainwright[5], R. Yoshino[4]

[1]*Centre de Recherches en Physique des Plasmas, Association EURATOM-Confederation Suisse, EPFL, 1015 Lausanne, Switzerland*

[2]*Triniti, Troitsk, Russian Federation*

[3]*RRC Kurchatov Institute, Moscow, Russian Federation*

[4]*Naka Fusion Research Establishment, JAERI, Naka, Japan*

[5]*Imperial College of Science, Technology and Medicine, London, UK*

[6]*Ass. EURATOM/ENEA/CREATE, DAEIMI, Univ. of Cassino, Cassino, Italy*

Abstract

Although linear response models are useful for feedback controller design, their linear time-invariant properties cannot simulate the evolution of a full plasma discharge. A suitable code for this purpose is DINA, which has now been benchmarked against a complete set of experimental data from TCV control experiments in both the time and frequency domains. Experimental measurements of the plasma equilibrium dynamic response to poloidal field coil voltage variations have recently been performed on the JT-60U tokamak. These results have been compared with the RZIP rigid current displacement model, previously validated on TCV, but enhanced for the work described.

1. DINA simulations of TCV

Considerable attention is being focused on the design of plasma position, current and shape controllers for the next generation tokamak-reactor designs such as ITER-FEAT. The development of a new control algorithm for a new plasma configuration will require numerical analysis prior to experimental tests to optimise experimental time. It is therefore necessary to have a validated tokamak plasma simulator to test any new proposed plasma controller design. A first requirement of such a tool is its ability to model a real experimental plasma evolution with sufficient accuracy. Considerable success had been obtained in modelling the stationary phase of TCV discharges using two linear models, RZIP and CREATE-L [1,2,3]. However, to simulate a full discharge we require a non-linear self-consistent model. DINA [4] is a tokamak plasma simulation code comprising a 1.5D axi-symmetric, time-dependent, resistive MHD and transport-modelling free boundary equilibrium solver in an externally imposed magnetic field and is a suitable candidate for such work. In this section the validation of the DINA code against an extensive set of TCV plasma equilibrium response experiments is presented.

Initial test simulations using the DINA code indicated that two technical improvements were useful. Firstly the feedback controller for these discharges has a high low-frequency gain to reduce any static offset. The feedback controller had to be initialised suitably at the start of the simulation to avoid a transient which could drive the simulation unstable and even end it prematurely, illustrated in Fig.1. Secondly, it is very difficult to adjust the poloidal flux consumption between an experiment and a simulation, since the latter did not model the transport in most of the cases. Modelling the transport would not have helped matching the data, since a long adjustment of the transport coefficients by trial and error would have been necessary to obtain even modest agreement. A pragmatic solution was therefore adopted, feeding back the toroidal resistance to agree with the experiment. This adjustment did not perturb the investigation into the dynamic equilibrium response which in most cases was assessed with the lowest frequency response (drift and offset) removed from both simulation and experimental data.

With these two improvements, 27 different discharges were simulated, with no adjustment of the DINA code, except for one minor numerical problem encountered for a particular discharge. Both limited and diverted plasmas were well modelled during the plasma current flat-top for the rejection of external square-wave PF coil voltage pulses. Examples of the comparison between TCV and DINA responses are shown in Fig.2. The agreement between the simulation and the experimental results was almost always within the noise width of the experimental data.

A complete single null diverted plasma discharge was also successfully simulated. The most significant difference between experiment and simulation was the penetration time of the poloidal flux, leading to a delayed onset of sawtoothing in the DINA simulation than in the experiment, Fig.3. Since the plasma loop resistance has been adjusted to the experimental data, this implies that the initial penetration of the poloidal flux does not follow the toroidal resistivity and that care should be taken in using this assumption when investigating the plasma current ramp-up phase. Different temperature profiles were used and the transport was enabled to confirm that this effect was not an artefact. The sawtooth frequency itself did vary according to the assumptions on the profiles, Fig.3.

Square pulse voltage stimulation of the OH1 and OH2 coils led to oscillations during the resulting experimental shape excursions, which could not be reproduced by linear simulations, shown in Fig.4 for the OH1 response. The oscillations seen in the vertical position are well reproduced by the DINA simulation. The envelope increases around 400msec, showing that the TCV closed loop has gone unstable, with a growth time of 200-400msec. After 100msec, the oscillations become damped, when the closed loop is stable again. This change in closed loop stability is attributable to the increased vertical field decay index which causes an excursion of the plasma elongation. The increase of elongation from 1.45 to 1.53 occurs at the same time that the closed loop is unstable. This observation is an example of non-time-invariant behaviour of the experiment and the simulation, which can never be simulated by linearised models, for which time invariance is assumed.

The complete set of 18 frequency stimulation experiments used to measure the open loop TCV plasma equilibrium response was also simulated in DINA and the results were analysed in an identical fashion to the experimental data [3]. In this more recent analysis, we used the coil voltages rather than the PF power supply demand voltages as the input signal, since this change actually renders the analysis more sensitive to differences between models, although being more noise prone. The frequency response of the DINA simulations agreed with the experimental results. The CREATE-L and RZIP models gave reasonable agreement as well, with the former showing fewer departures from the experimental results than the latter.

2. JT-60U Experiments

The method [3] used on TCV to measure the open-loop plasma equilibrium response during the closed-loop control of the vertically unstable plasmas has been repeated on JT-60U. The RZIP model of JT-60U has been re-derived using a clean Lagrangian approach. This removed a previous asymmetry in the determining equations concerning the radial derivative of the plasma resistance and the coupling between major radius and plasma current, but left most terms unchanged, see the equation at the end of the paper with the same conventional terminology as in [3]. A series of experiments was then performed with no plasma, in an Ohmic plasma and an NBI-heated plasma, using multi-sine (5 frequencies) excitation of the 5 PF coil voltages in the range 4-80Hz, to determine the dynamic response of all diagnostics. The plasma-less model was fine-tuned to compensate for external circuitry and any constructional differences, to a precision of a few percent, beyond simple measurement accuracy. Different cost functions were explored to define a best tuning. This procedure was necessary to avoid biasing the measurements with plasma and attributing any differences found to plasma model errors. The open-loop plasma response agreed well with the RZIP model, except for the plasma current response. Varying the plasma resistance derivative in the model showed that this small term is not experimentally determined by these experiments. Calibrating the values of the plasma inductance and plasma resistance in the model to agree with the experimental data showed that the

effective resistance is much higher than the loop resistance and that the effective inductance is slightly lower than the nominal low frequency inductance. It is assumed that these observations can be explained by a skin-effect. The resulting agreement between the experimental and modelled dynamic responses is shown in the Bode diagrams in Fig.5 for the most important responses for designing a controller, namely the control parameters. The plasma-less response is shown as crosses for the data and thick lines for the model. The plasma responses are indicated as circles for the data and thinner lines for the RZIP model.

Finally, the closed loop operation of JT-60U has been successfully simulated using the RZIP model and a linearised approximation of the JT-60U feedback controller. Empirical fine-tuning of this controller has been started to reduce some of the residual cross-couplings seen in the data.

Acknowledgements

Thanks go to the TCV and JT-60U teams without whom the experimental results would not be comparable with the models. Two of the authors (RK, VL) thank the CRPP for their hospitality during visits to TCV. Two of the authors (JBL, AS) thank JAERI-Naka for their hospitality during visits to JT-60U. This work was partly supported by the Swiss National Science Foundation and three of the authors (DJNL, AS, JPW) were partly supported by the United Kingdom EPSRC.

References

[1] Villone F., Vyas P., Lister J.B., Albanese R., Nuclear Fusion **37** (1997) 1395

[2] Vyas P., Villone F., Lister J.B., Albanese R., Nuclear Fusion **38** (1998) 1043

[3] Coutlis A. et al., Nuclear Fusion **39** (1999) 663

[4] Khayrutdinov R.R., and Lukash V.E., J. Comp. Physics **109** (1993) 193

RZIP Equation

$$\begin{bmatrix} L_s & \left.\frac{\partial M_{sp}}{\partial z}\right|_0 & \left.\frac{\partial M_{sp}}{\partial R}\right|_0 & M_{sp}^0 \\ \left.\frac{\partial M_{sp}}{\partial z}\right|_0 & \left.\frac{\partial^2 M_{sp}}{\partial z^2}\right|_0 \frac{I_s^0}{I_p^0} & \left.\frac{\partial^2 M_{ps}}{\partial z \partial R}\right|_0 \frac{I_s^0}{I_p^0} & 0 \\ \left.\frac{\partial M_{ps}}{\partial R}\right|_0 & \left.\frac{\partial^2 M_{ps}}{\partial z \partial R}\right|_0 \frac{I_s^0}{I_p^0} & \left(\frac{1}{2}\left.\frac{\partial^2 L_p}{\partial R^2}\right|_0 + \left.\frac{\partial^2 M_{ps}}{\partial R^2}\right|_0 \frac{I_s^0}{I_p^0}\right) & \left(\left.\frac{\partial L_p}{\partial R}\right|_0 + \left.\frac{\partial M_{ps}}{\partial R}\right|_0 \frac{I_s^0}{I_p^0} + 4\pi\mu_0 \frac{S}{l^2}\beta_p^0\right) \\ M_{ps}^0 & 0 & \left(\left.\frac{\partial M_{ps}}{\partial R}\right|_0 \frac{I_s^0}{I_p^0} + \left.\frac{\partial L_p}{\partial R}\right|_0 + 4\pi\mu_0 \frac{S}{l^2}\beta_p^0\right) & L_p^0 + 4\pi\mu_0 \frac{S}{l^2}\beta_p^0 R^0 \end{bmatrix} \dot{\vec{x}} +$$

$$\begin{bmatrix} \Omega_s & 0 & 0 & 0 \\ 0 & 0 & 0 & 0 \\ 0 & 0 & 0 & \left.\frac{\partial \Omega_p}{\partial R}\right|_0 \\ 0 & 0 & \left.\frac{\partial \Omega_p}{\partial R}\right|_0 & \Omega_p^0 \end{bmatrix} \vec{x} = \begin{pmatrix} \delta V_s \\ 0 \\ -2\pi\mu_0 \frac{S}{l^2} I_p^0 \dot{\beta}_p \\ -4\pi\mu_0 \frac{S}{l^2} I_p^0 R^0 \dot{\beta}_p \end{pmatrix}$$

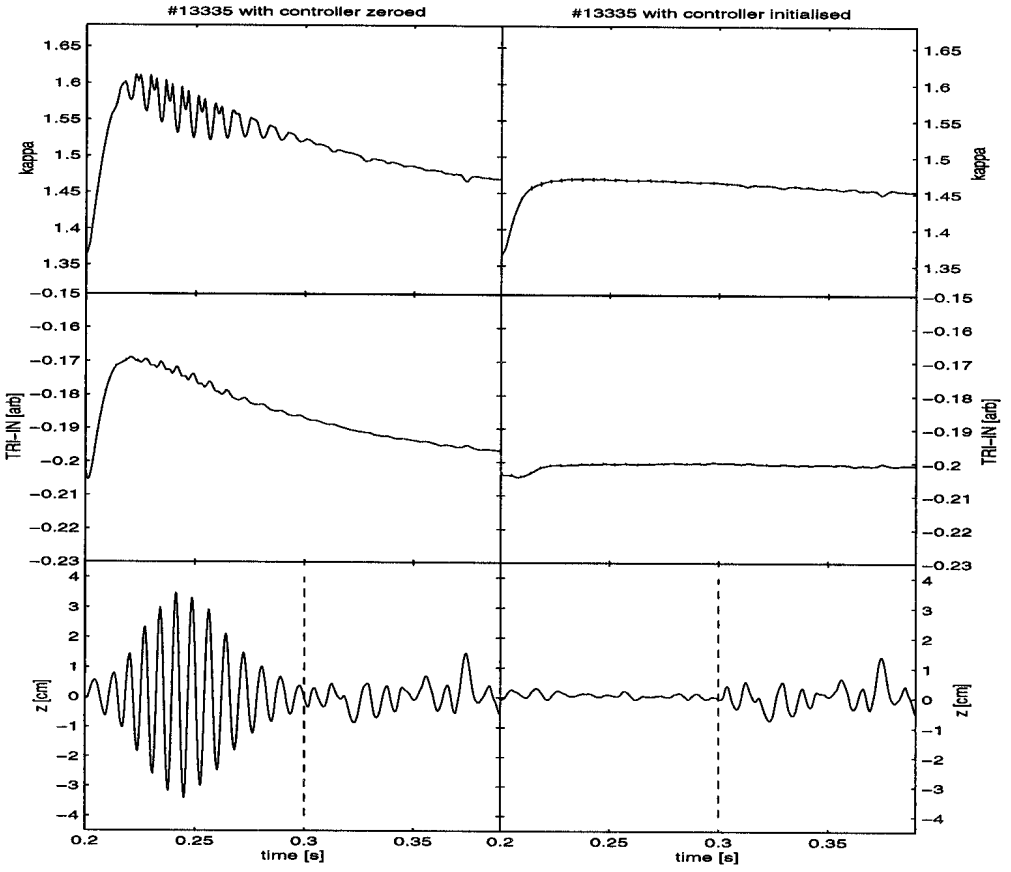

Figure 1 Improvement to the controller initialisation caused a significant reduction to the transients at the start of the DINA simulation (right). Uninitialised (left), the transient included an increase to the vertical field decay index and hence to the elongation (top trace), resulting in an anomalous vertical instability showing up on the vertical movement trace (bottom) which caused a failure of the simulation in early tests. The middle trace shows the excursion of the control parameter for elongation. The start of the stimulation is indicated as a vertical dotted line.

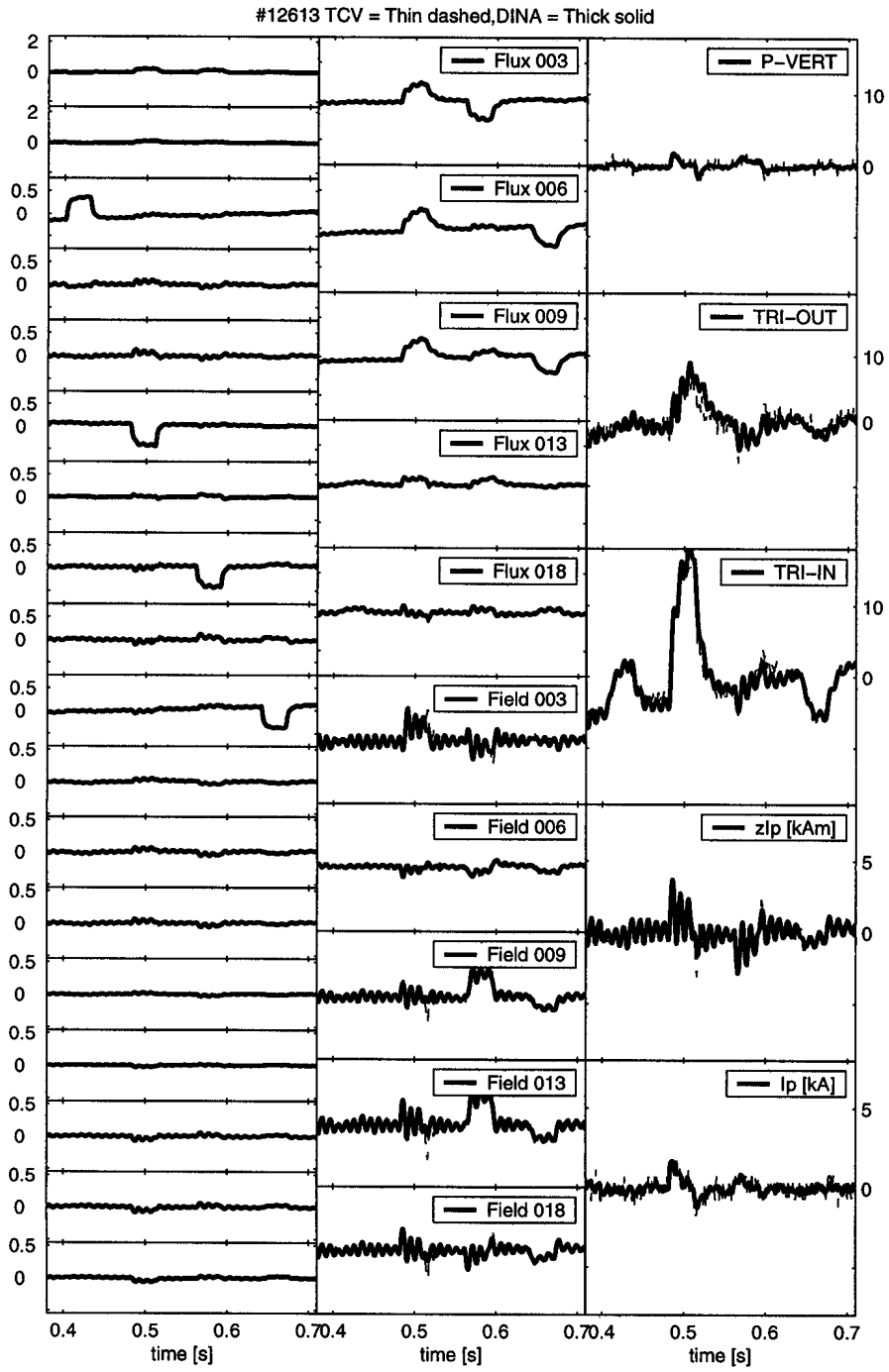

Figure 2 Simulation of a diverted off-centred plasma, using separate E1, E4, E6, E8 coil stimulations in a single pulse. The signals are shown detrended: (left column) all 18 external PF coil currents, OH1, OH2, E1 to E8, F1 to F8; (middle column) flux loops #3,6,9,13,18, magnetic probes #3,6,9,13,18; (right column) the five feedback control parameters.

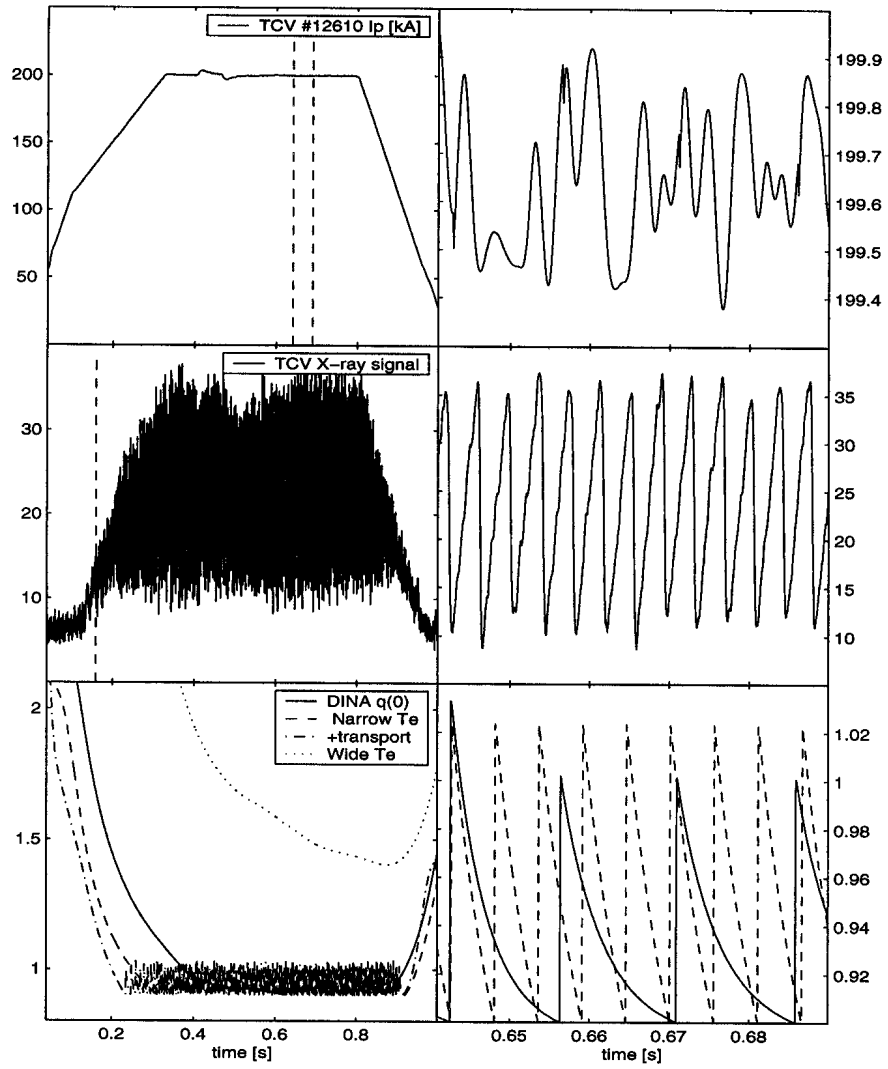

Figure 3 Comparison between DINA simulation and TCV for the evolution of the sawtooth activity: left, the full pulse showing, from top to bottom: TCV Ip, TCV soft X-ray signal, DINA q(0); right, an expanded view of the same signals.

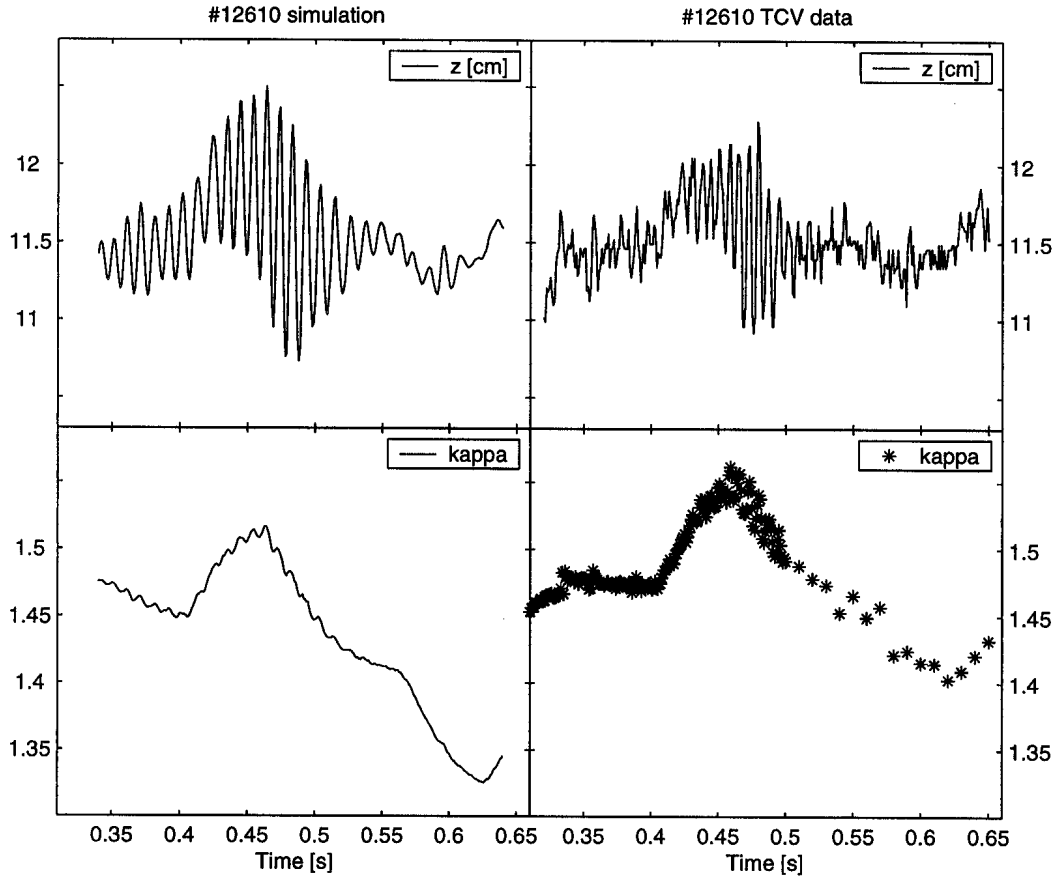

Figure 4 Comparison between TCV (left) and the DINA simulation (right) for a large excursion due to a square voltage pulse OH1 stimulation. The vertical position goes closed loop unstable and returns to closed loop stable once the elongation is reduced.

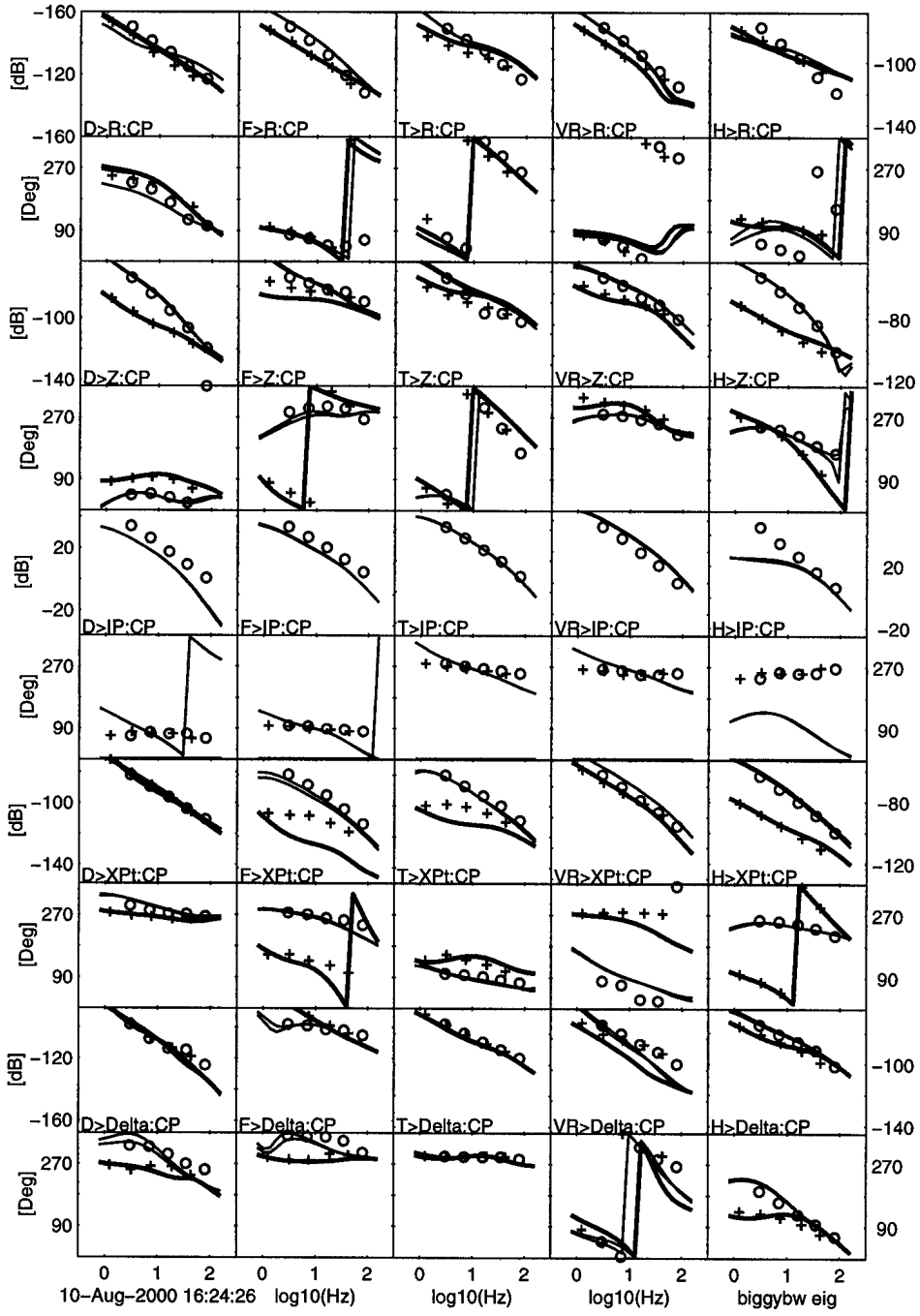

Figure 5 Selected open-loop responses from the JT-60U tokamak. The heavy lines and (x) are the plasma-less model and data. The thin lines and (o) are the plasma data.

Presented at 21st Symposium on Fusion Technology, September 11-15, 2000 Madrid, Spain

Self-Field Effects in Large Superconducting Cables for ITER

Alexander Anghel
Centre de Recherche en Physique des Plasmas
Association EURATOM
CH-5232 Villigen, Switzeland
alexander.anghel@psi.ch

Preliminary results of a new stochastic model for the self-field effect in large Cable In Conduit Conductors (CICC) are presented. We show that the electric properties of CICC can be inferred by using only one (arbitrary and not necessary exact) strand trajectory. By applying a different integration technique (Lebesgue) of the electric field along a strand and the Central Limit Theorem we show that all the information is contained in a probability distribution function of one strand trajectory. We show that the exact critical current of a cable with perfect joints is close to that based on the strand critical current at peak field if there is no current transfer between strands. With perfect current transfer the cable critical current approaches the ideal (free strand) value at high fields.

1. INTRODUCTION

The full size CICC model conductors for ITER, like those developed for the Central Solenoid (CS) and Toroidal Field (TF) coils are currently investigated at the SULTAN facility at CRPP, Villigen, CH. One of the most important parameter measured is the critical current dependence on field and temperature. The samples, exposed to different back-ground fields are charged-up to currents as high as 100kA. In such testing conditions, the self field of the sample cannot be neglected. A similar effect exists also for large magnets.

The CICC are made of a great number ($\sim 10^3$) of superconducting strands (NbTi or Nb_3Sn). In order to reduce the AC losses in the cable and to improve the mechanical stability, the strands are twisted at different stages according to some predefined scheme e.g. 3x4x4x4x6. Each strand travels along the cable and is exposed to different magnetic fields because the field in the cable cross-section is not uniform. It is therefore difficult to assess a unique magnetic field for the cable. Usually one checks with the background, the average or the peak field. Surprisingly but not yet explained, the fits with the peak field are relatively good, although it is known that due to twisting only a fraction of the strand trajectory is at the peak field. We will try to explain this paradox here. Besides the self-field there are other factors affecting the DC performance like the non-uniform current distribution and heat transfer. The effect of the non-uniform current distribution will be considered here only in two limiting cases: no current transfer and perfect current transfer assuming no current imbalance from the joints. The heat transfer and the real non-uniform current distribution taking also the joints into account will be presented elsewhere.

2. THE AVERAGE ELECTRIC FIELD OF ONE STRAND

Generally, one should always distinguish between the singular-strand E-I characteristic and the strand E-I characteristic when the strand is member of a cable. The E-I characteristic of a singular strand as a function of the strand current I, is given by the power law

$$E(I) = E_c\left(\frac{I}{I_c}\right)^n \tag{1}$$

where I_c is the critical current, a known function of field and temperature and n=30-35 (NbTi) or 15-20 (Nb3Sn) is the index of the power law. For a strand in a cable, due to the non-uniform field distribution in the cable cross section and inhomogeneous current distribution among the strands we are constrained to define an average electric field taken over a given length L along the real strand trajectory in the cable. Usually L is taken as the length over one or several twist pitches of the last stage. Denoting by C_i the strand trajectory and by s_i the arclength we have

$$\overline{E}_i(I) = \frac{I}{L}\int_{C_i} E\left(\frac{I}{I_c(s_i)}\right)^n ds_i \tag{2}$$

where $I_c(s_i) = I_c\left(B(\vec{r}_i, I_t), T\right)$ is the critical current, a function of the local field and temperature, I_t -the total cable current and the strand current variable is I.

The ideal strand trajectory is described by the 2D-vector $r_i(x_i(z),y_i(z))$ if the curve is parameterized by the z coordinate. The general equations for x_i and y_i (winding law) are

$$x_i(z) = \sum_{n=1,S} r_n \cos\left(\frac{2\pi z}{p_n^*} + \varphi_{i,n}\right)$$
$$y_i(z) = \sum_{n=1,S} r_n \sin\left(\frac{2\pi z}{p_n^*} + \varphi_{i,n}\right) \qquad (3)$$
$$\frac{1}{p_n^*} = \frac{1}{p_n} + \sum_{m=n+1}^{S} \frac{\xi_m}{p_m}$$

where S is the number of stages, r_n are the radii of gyration in each stage, p^*_n are the effective twist pitches of each stage and the initial phases $\phi_{i,n}$ fix the initial position of the strand. It is through this phases that we distinguish between different strands i.e. there are exactly N_s combinations where N_s is the number of strands. The different terms in the sums above represent rotations of groups of strands at each stage level. The cabling process (% of torsion, back-twist, etc.) is introduced via coefficients ξ_m. For full torsion we have $\xi_m = 1$, for full back-twist $\xi_m = 0$. Similar relations describe the real trajectory, but now r_n are functions of z. Unfortunately, this dependence is much too complicated to be described by a simple equation and numerical methods have been developed to calculate the real strand trajectory [1, 2]. Although very elegant in concept, the codes are time consuming and are therefore not suitable for rapid calculations or parametric studies.

We construct our analytical form for the strand trajectory by keeping the twist-pitches at the nominal values and selecting the values of r_n as: $r_5=(r_c-r_h)/\lambda+r_h$, $r_4=(r_c-r_5)/\lambda$, $r_3=r_4/\lambda$, $r_2=r_3/\lambda$ and $r_1=r_2/\lambda$ where r_c and r_h are the cable and hole radii. Imposing the condition $\Sigma r_n=r_c$, one get the nontrivial solution $\lambda=1.926$. Eq.(3) is then used to model the strand trajectory. Eventually we added a random term of the order of the strand diameter to model the strand rearrangements during compaction, which is possible at the level of the first two stages. Simulation have revealed that, even in the absence of the random term, the strand trajectories are very haphazardous due to the cumulative effect of overlapping rotations at different stages.

3. From Path Integral to Statistical Average

The average electric field of a strand in a cable is a path integral over the strand trajectory. The strand trajectories are pretty discontinuous, as we have seen before. Additionally, in some regions we can have $I_c(B)=0$ and the integrand in Eq.(2) diverges. Under this conditions it is almost sure that the line integral in (Eq.2) do not exists as a Riemann integral. Fortunately, there exist another important technique of defining and doing integrals, which works even for completely discontinuous functions. This is the Lebesgue integral [3]. Applying this technique we get the following expression for the average electric field of a strand

$$\bar{E}_i(I) = \sum_{\alpha} E_c\left(\frac{I}{I_c(B_\alpha)}\right)^n f_\alpha^i = \sum_{\alpha} E_i^\alpha f_\alpha^i \qquad (4)$$

where f_α^i is the fractional number of positions along the trajectory for which $B<B(s_\alpha)<B+dB$ and can be interpreted as a probability distribution. α is the running index over an arbitrary partition of the interval $[0,L]$ Each strand will have, in a strict sense, his own probability distribution but our calculations show that they do not differ too much in statistical sense and we will see later that this do not count for a cable with a large number of strands.

If the background magnetic field does not vary substantially with z and if the small dependence of the self field on the y-coordinate is neglected then $B(s_\alpha)$ is a function of only the x-coordinate. For example in the case of a single conductor in a uniform background field B_b we have

$$B(s_\alpha) \cong B(x(z), I_t) = B_b + \frac{\mu_0 I N_s}{2\pi r_c^2} x(z) \qquad (5)$$

In this case the distribution function f can be calculated as the distribution of $x(z)$ i.e. as the fractional number of x-coordinates of the strand trajectory projected on the cable cross section with $x<x(z)<x+dx$, as illustrated in Fig.1.

4. Average Electric Field in the Cable and the Central Limit Theorem

It is generally accepted that the electrical field of a cable composed of N_s strands is given locally by

$$E_{cable} = \frac{1}{N_s} \sum_{i=1,N_s} E_i \qquad (6)$$

If we treat E_i as a random variable with probability distribution f^i then the local cable electrical field is the sum of N_s random variables E_i, one for each strand and is on its turn also a random variable. We look now for the distribution function of E_{cable} and even more

important for its average. The answer is easy if we remember the Central Limit Theorem (CLT) [4]. With our notation it states that the cumulative distribution function of the N_s random variables E_i with mean $\overline{E}_i$ and variance σ_i is the normal (Gaussian) distribution for large N_s. In other words, E_{cable} is normal distributed with the average $\overline{E}_{cable} = \overline{E}_i$ and variance $\sigma_{E_{cable}} = \sigma_i / \sqrt{N_s}$. Theoretically the CLT holds exactly for $N_s \to \infty$, but practically an N_s of 10-100 is already enough for the cumulative distribution to show the first Gaussian characteristics. Therefore for large cables with N_s~*1000* the result holds more than satisfactorily. This demonstration is not absolutely rigorous because we did not said anything about how the different trajectories are correlated. If they are strong correlated, i.e. not independent, the CLT does not hold. It is obvious that at the level of individual triplets the strands should be correlated in principle. A weak correlation is however admitted by CLT. These aspects and the consequences can be discussed only in a more general frame of ergodic theory.

From this discussion the following recipe for calculating the average electric field in a cable emerges:

Take an arbitrary strand in a given cable and calculate the distribution function associated with this particular trajectory. It could be the exact or an approximation of the exact trajectory. Then with probability almost one, the cable average electric field is the strand average electric field calculated with this probability distribution.

This is our main result. It implies that there is not necessary to calculate exactly all strands trajectories, integrate the electric field along them and then averaging in order to find the electric field of the cable. The CLT states that it is enough to calculate, even approximately, one trajectory, to evaluate the average electric field of the strand and then asses, with probability almost one, this value to the average electric field of the cable.

5. RESULTS

In the present work we present some results obtained with this new analytical model. The main points of our model are:

1) We found first an approximate form of the strand trajectory based on Eq.(3) by keeping the twist pitches at the nominal (cabling) values and choosing values for r_n such that the strand trajectory does not overlap the cable boundaries (outer radius and central hole). To this we add a uniformly distributed random term of the order of the strand diameter.

2) The probability distribution function is then calculated for this particular strand trajectory. Due to the simple analytical form of the strand equation, the distribution function for different strands can be compared. Also, different combinations of twist pitches and/or comensurability-incomensurability effects can be analyzed.

3) The electrical field is calculated using Eq.(4). By imposing the condition $E(I)=E_c$, the critical current of one strand in the cable is determined.

4) Repeating the above procedure at different background fields the whole field dependence of the critical current can be calculated.

5) Based on the CLT the results can be extrapolated to the full cable. The cable current is then simply the strand current times the number of strands.

To illustrate our model we consider here the case of the NbTi prototype cable (TOSCA Bus-Bar) tested recently in the SULTAN facility. It has 1152=3x4x4x4x6 strands 0.81mm in diameter. The main cable dimensions are: outer radius $r_c=19.2mm$, hole radius $r_h=6mm$. The strand trajectories were described by Eq.(3) with $p_1=45mm$, $p_2=85mm$, $p_3=125mm$, $p_4=160mm$ and $p_5=410mm$ and properly chosen r_n. The critical current of the isolated strand $I_c(B)$ is modeled with the standard correlation for NbTi. An index $n=35$ is assumed in the power law for the strand.

A typical strand trajectory calculated for $L=p_5$ is illustrated in Fig. 1. The corresponding distribution function is presented on the top of Fig. 2. The change in the distribution function if one goes to $L=10p_5$ is shown on the bottom. Both distributions are compared to the continuous distribution function obtained assuming that the strand trajectory is uniformly distributed in the cross section of the cable i.e. the fraction of points between x and $x+dx$ is proportional to the area. One can see that for large L the distribution function of one strand converges towards the continuous distribution, but about 10 twist pitches are necessary to achieve a reasonable precision. Therefore care should be taken when using the continuous distribution at short length.

The results of the calculation of the electrical field at $T=4.2K$ and $B_b=6T$ for $E_c=10\mu V/m$ are shown in Fig.3. Here, besides the average electric field calculated with Eq.(4), the calculation at the peak field and at the background field are shown for comparison. It can be seen that there is a reduction of about 50% in the critical current as compared to the critical current at background field and that the critical current calculated at peak field is only about 10% lower.

The reason for this 10% difference is that only the few last terms in Eq.(4) are contributing to the

electric field for large n (n~30) i.e. the high-field (close to peak-field) terms. This explains the peak-field paradox.

The critical current calculated with Eq.(4) represents obviously the case with no current transfer between the strands i.e. each strand keeps its imposed current at all possible fields in the cross-section. It is the worst case and therefore a lower bound on the real critical current of a cable. An upper bound can be calculated assuming a cable with perfect current transfer. In such a cable, each strand in each cross-section carries a current equal to the critical current at the local field. The excess current is (perfectly) transferred to other strands, which are at lower field (in the same cross-section) and then back to the initial strand when itself is (in other cross-section) at lower field. The upper bound of the critical current can be defined as

$$I_{upper}(I) = E_c\left(\frac{I}{I_{c\_avg}}\right)^n$$
$$I_{c\_avg}(I) = \sum_{\alpha} I_c(B_\alpha) f_\alpha \qquad (7)$$

The dependence of the lower and upper bound critical currents on the background magnetic field is presented in Fig.4. It is obvious that the critical current curve of a cable will be somewhere in-between the two curves, closer to the lower one if the inter-strands transversal resistance is high and closer to the upper one if the strands have good electrical contact. The upper-bound curve converges to the isolated strand critical line at high fields. At low fields it deviates due to the field inversion in the cable cross-section in the region where the self-field is higher than the background field. The curve for the critical current calculated at peak field is about 10% lower than the lower bound. The variances of E at $I=I_c$ are all about $11.4E_c$ in the whole field range and for the whole cable it is $0.336E_c$, an increase in precision of the order $\sqrt{N_s}$.

6. Conclusions

We presented a simple method to evaluate the critical current of a large CICC under the influence of the self-field effect. The influence of current transfer is considered in the limiting cases of perfect and no current transfer. The current imbalance effect of imperfect joints is neglected i.e. the joints are assumed to be perfect. The method avoids using complicated and time consuming numerical codes to evaluate the strand trajectory of all the strands in the cable (~10^3). It can be easily implemented as a spreadsheet document and is well suited for cable design or parametric studies. It can be extended to include the temperature effect and the inhomogeneous current distribution. Lorenz force effect can be accounted by applying a deformation on the strand trajectory proportional to the field and strand current.

Fig.4 synthesizes our results. It can be viewed as a kind of phase diagram. The upper line represents the ideal cable with no self-field effect, perfect joint and perfect current transfer. The second line is the upper bound calculated by weighting appropriately the self-field effect in the cable and assuming perfect current transfer. Again a perfect joint is assumed. At high fields the two lines overlap. The first of the two bottom lines is the lower bound on the critical current with no current transfer and perfect joint. It overlaps pretty well with the line representing 50% of the ideal cable curve. The lower-bound curve is close to the peak field line. Under these lines is the region of current imbalance caused by imperfect joints. From this diagram it can be seen that the DC cable performance can be increased only by manufacturing better joints and increasing the current transfer.

The basic idea of the method is that ensemble average of the electric field of a cable i.e. the average over all strands can be replaced by the zaverage over one strand or in other words the statistical average by the sample average. We presented here only an heuristic proof based on the CLT. A more rigorous proof is possible, based on the concept of ergodicity [5] and will be published soon.

References

[1] Y. J. Chen and J. P. Freidberg, A Method for Modeling the Winding Pattern of a Large Scale Superconducting Cable, IEEE Trans. on Magn. 32 (1996) pp. 5145-5147

[2] T. Schild, D. Ciazynski and S. Court, Effect of Actual Cabling Pattern on the Critical Current of Multistage CIC, Advances in Cryogenic Engineering, 46B (2000) pp. 1051-1058

[3] www.mathworld.wolfram.com, key words: Lebesgue integral, Lebesgue measure

[4] N.G. van Kampen, Stochastic Processes in Physics and Chemistry, North-Holland PL, Amsterdam, 1981, pp. 27-31.

[5] A. Papoulis, Probability, Random Variables and Stochastic Processes, McGraw-Hill, 1984 pp. 245-254.

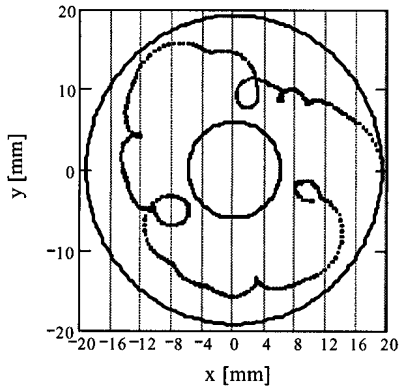

Figure 1. Projection of the strand trajectory on the cross-section of the cable. In order to determine the probability distribution the x axis is partitioned in intervals of width d_s and the number of points falling in each interval is counted.

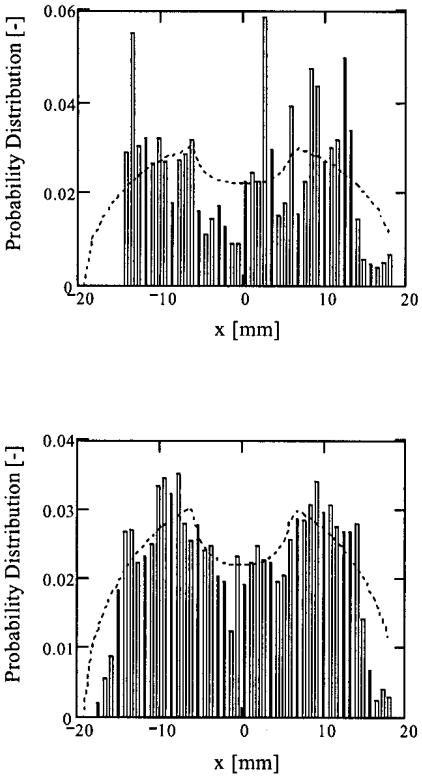

Figure 2. Probability distribution of the strand trajectory. Over one twist pitch (top) and ten twist pitches (bottom). The dashed line is the probability distribution for uniformly distributed strands in the cross-section.

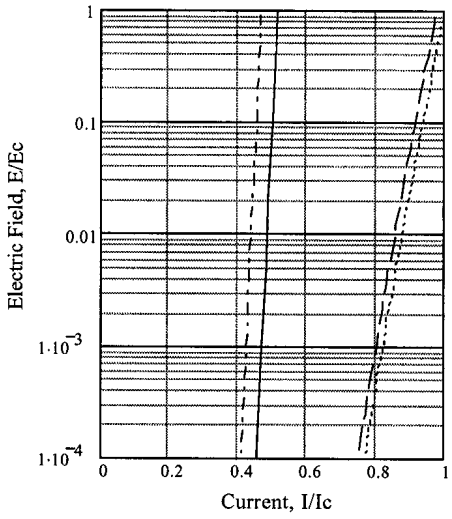

Figure 3. Electric field in cable as a function of strand current. Peak-field (dash-dot), averaged with probability distribution (line), perfect current transfer (dash) and background field (dot).

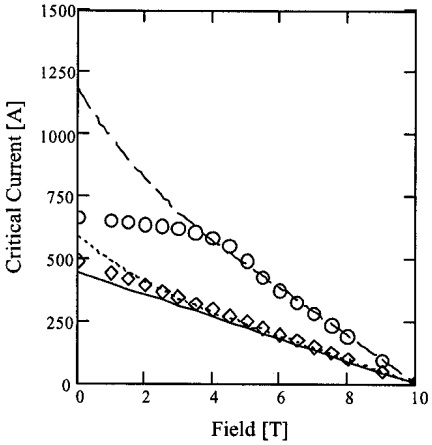

Figure 4. Upper and lower limit of strand critical current in the cable as a function of background magnetic field. No current transfer (diamond), perfect current transfer (circle). For reference the single strand critical curve is shown at 100% (dash) and 50% (dot). The critical current at peak-field is represented by the continuous line.

Pressure Drop And Helium Inlet In ITER CS1 Conductor

Pierluigi Bruzzone

CRPP-Technologie de la Fusion, 5232 Villigen-PSI, Switzerland

Abstract. A number of pressure drop measurements have been carried at CRPP on a section of ITER cable-in-conduit conductor, using pressurized water at room temperature. The longitudinal friction factor is deduced for the strand bundle area and the central hole. Two layouts of radial Helium inlets have been investigated and the measured radial pressure drop is assessed in terms of the equivalent conductor length producing the same pressure drop in axial direction.

1. Introduction

For magnets wound by forced flow conductors, it is convenient to make the distance between coolant inlet and outlet ("hydraulic length") as short as possible to reduce the pressure drop and increase the coolant speed. In layer wound coils, the hydraulic inlet/outlet can only be placed at the end of the layers and the electrical connections (joints) are also used as hydraulic inlet/outlet. In the pancake wound coils, the electrical connections between conductor sections may be conveniently placed at the outer radius, where the magnetic field is weaker. The hydraulic inlet is at the pancake transition at the inner radius. The coolant stream splits into the two pancakes and the electrical connections are used as hydraulic outlets. This arrangement offers the advantage of a short hydraulic length (half of the conductor sections) and provides the lowest operating temperature at the highest field.

The fusion magnets planned for ITER are built from double pancakes, with coolant inlet at the pancake transition. However, the ITER Model Coils have been built as layer winding (CSMC) and single pancake stack (TFMC), with the hydraulic inlet/outlet always placed at a conductor joint. The following investigations are devoted to the hydraulic behavior of the radial coolant inlet for the ITER conductor, with the aim to assess the pressure drop at the inlet versus the axial pressure drop per unit meter of conductor.

2. Sample Layout and Test Set-up

A section of ITER CS1 conductor [1], left from the winding of the second layer of the inner module of the CS Model Coil (CS1.2 B), is used for the hydraulic test. The ends of the conductor section have been cut by electronic erosion to obtain a proper cut, without strand smearing and local variation of the Helium cross section. The geometry data of the conductor are summarized in Table 1 [2, 3]. For the wet perimeter in the strand bundle, the full strand perimeter is accounted.

The axial pressure drop measurements have been carried on a straight, 6 m long conductor section. The sample has been later cut to 1 m length to extend the range of mass flow rate. The axial test has also been repeated after blocking the central hole by a rubber pipe, restricting the flow to the bundle area. The rubber pipe, with diameter slightly larger than the central hole, is pulled through the conductor and is sealed at the side of the fluid outlet.

Table 1. Geometric data of Conductor CS1.2 B

Description	*Symbol*	*Formula*	*Value*	*Source/Method*
Cable space average Diameter	d_{cs}	-	38.99 mm	Measured on test sample
Cable space area	A_{cs}	$\pi(d_{cs}/2)^2$	1194 mm^2	From above data
Subcable wrap perimeter	P_{sw}	-	305 mm	From Nicollet [2]
Subcable wrap cross section	A_{sw}	$P_{sw}\cdot 0.1$	30.5 mm^2	From above data
Outer wrap perimeter	P_{ow}	-	220 mm	Measured on test sample
Outer wrap cross section	A_{ow}	$P_{ow}\cdot 0.1$	22 mm^2	From above data
Spiral cross section	A_{sp}	-	24 mm^2	From Nicollet [2]
Spiral half perimeter	P_{sp}	$A_{sp}/1$	24 mm	From above data
Spiral inner/outer diameter	d_{spi}/d_{spo}	-	9.8/11.8 mm	Measured on test sample
Mean twist angle in strands	$\cos\theta$	-	0.925	From ITER QA [3]
Strand diameter	d_{st}	-	0.81 mm	From ITER QA [3]
Twisted strand cross section	A_{st}	$1152\cdot\pi(d_{st}/2)^2/\cos\theta$	642 mm^2	From above data
Helium cross section overall	A_{HeOv}	$A_{cs}-A_{st}-A_{sw}-A_{0w}-A_{sp}$	472 mm^2	From above data
Helium in central hole	A_{HeH}	$\pi(d_{spi}/2)^2$	76 mm^2	From above data
Helium in bundle	A_{HeB}	$A_{HeOv}-A_{HeH}$	396 mm^2	From above data
Void fraction in bundle	ν_B	$A_{HeB}/(A_{cs}-\pi(d_{spo}/2)^2)$	36.5 %	From above data
Wet perimeter	P_w	$1152\pi d_{st}/\cos\theta+P_{sw}+P_{ow}+P_{sp}$	3.61 m	From above data
Av. hydraulic diameter overall	d_{ov}	$4A_{HeOv}/P_w$	0.523 mm	From above data
Av. hydraulic diameter in bundle	d_B	$4A_{HeB}/P_w$	0.438 mm	From above data

For the radial pressure drop, two layouts of Helium inlet have been compared. In one case, a plain hole, ø = 16 mm, has been drilled on one side of the jacket. To avoid damage in the cable, the hole must be finished by manual tools. The outer cable wrap is removed by a grinding tool and a pipe, $ø_{in}$= 16 mm, is welded to the jacket, see Fig. 1 left. In a second, more sophisticated design, a 200 mm long section of jacket is fully removed by a milling machine and replaced by two half shells with machined longitudinal and radial channels to improve the fluid penetration through the strand bundle and avoid stagnant Helium regions. The 8 longitudinal and 5 radial channels, see Fig. 1 right, have a cross section of 3 x 1.8 mm. The outer cable wrap is removed over the 200 mm, but the subcable wraps are maintained. After welding the shells together and to the jacket, the cable inside the shells is fully supported (no gap).

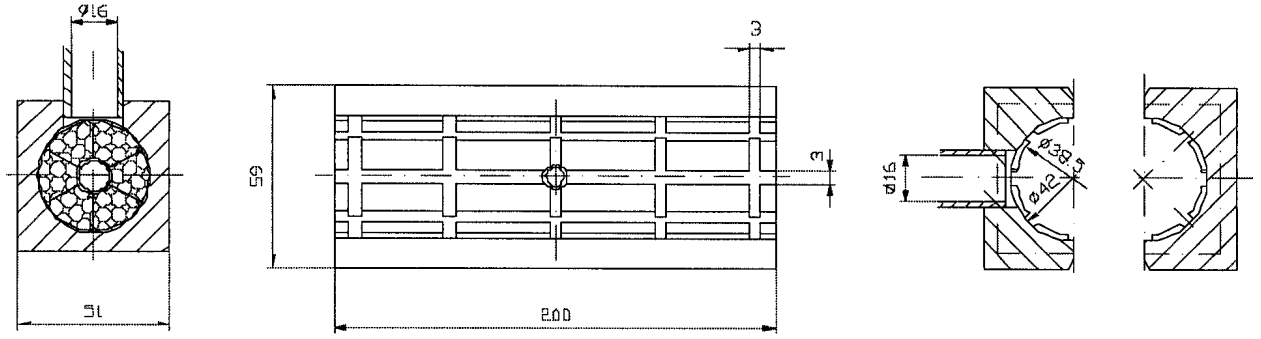

Figure 1. The two Helium inlet layouts: the plain hole in the jacket, ø = 16 mm (left) and the steel halves with machined radial and longitudinal channels (right)

Table 2. Operation parameters for CS1.B conductor

	CS Model Coil		Test at CRPP	
Temperature	≈ 5 K		28 C	
Fluid	Helium		Water	
Density, kg/m^3	141.1		996.2	
Viscosity, Pa·s	$4.45 \cdot 10^{-6}$		$822 \cdot 10^{-6}$	
Inlet pressure, bar	≈ 9		≈ 8	
Mass flow rate, kg/s	$0.007_{Overall}$	$\approx 0.003_{bundle}$	$0.85_{Overall}$	0.53_{bundle}
$\dot{m}/\eta$, kg/Pa·s^2	$1573_{Overall}$	674_{bundle}	$1034_{Overall}$	644_{bundle}

Pressure drop measurements on forced flow conductors must be done in the relevant range of Reynold numbers. The option to use supercritical Helium at the nominal operating conditions (mass flow rate, pressure and temperature) must be discarded when a short conductor length is measured: the pressure drop per meter length is in the order of one *mbar* and a test on a few meter long conductor section would be affected by severe accuracy problems. To obtain relevant Reynold numbers with Helium at room temperature, a very large mass flow rate is necessary, due to the very small density [4]. Using Nitrogen at room temperature, with seven-time higher density than Helium, it is easier to achieve high Reynold numbers [5]. However, large pressure and temperature variations occur from inlet to outlet, and the result assessment must be done using density and viscosity values averaged over a broad range of pressure and temperature. A convenient way to achieve high Reynold numbers and significant pressure drop in short sections of forced flow conductors is to use pressurized water at room temperature [6]. The temperature is constant and hence the density and the viscosity are constant too in a liquid, allowing good accuracy in the results.

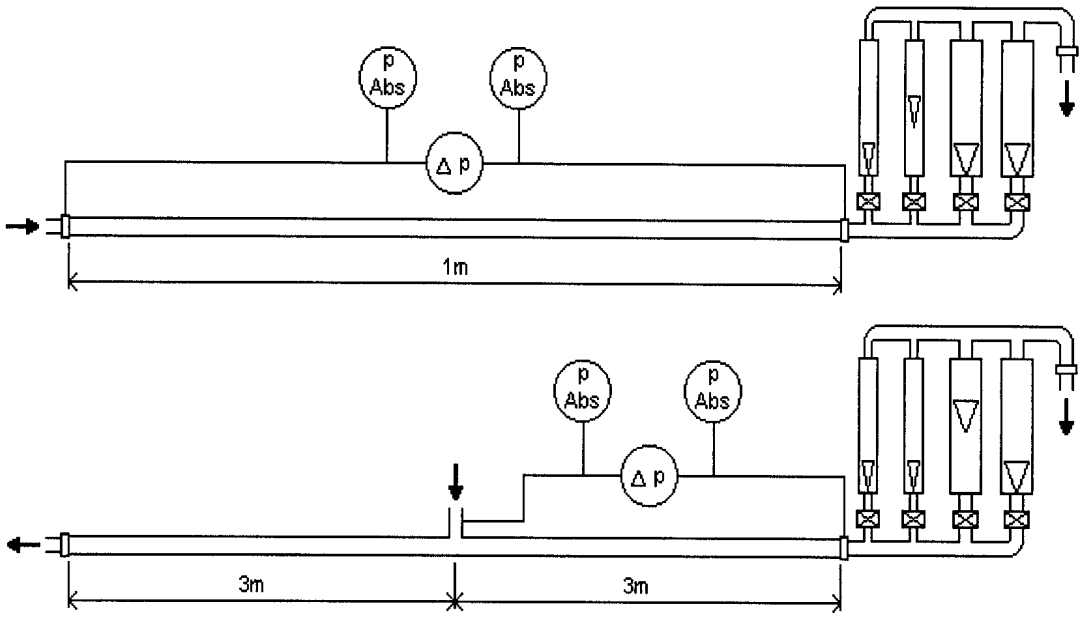

Figure 2. Schematic experimental set up for axial (top) and radial (bottom) pressure drop tests

At CRPP, the pressure drop measurements have been done using a closed circuit of de-mineralized water at 28 C. The nominal pressure of the circuit is 11 bar. With the largest mass flow rate, the actual pressure drop available at the sample is in the range of 5 bar. The Table 2 compares the parameters of the test at CRPP and the operating conditions of the CS Model Coil. As the conductor geometry is identical, the comparison can be done in terms of the mass flow rate divided by viscosity, $\dot{m}/\eta$, instead of the Reynold number, $\mathrm{Re} = \dot{m}d/A_{He}\eta$ (in a conductor with dual

channel the assessment of the hydraulic diameter, d, is quite arbitrary). Due to the high viscosity of the water at 28 C and the limited water flow (pressure) of the circuit at CRPP, the CSMC operating $\dot{m}/\eta$ is obtained only with the central channel closed: for the overall conductor (central channel open) an extrapolation to the actual $\dot{m}/\eta$ value is acceptable.

The schematic arrangement of the test set-up is shown in Fig. 2 for both axial and radial pressure drop measurements. The water flow rate is measured by four, parallel operated floating ball flow meters, ranging up to 3000 l/hrs, with overall accuracy better than 5%. The pressure drop is measured between inlet and outlet by two differential pressure devices ranging up to 0.7 and 1.5 bar. For larger pressure drop, the read-out of two absolute pressure meters is used. The pressure meters overlap with good agreement over a broad range.

3. Results Discussion

The test results are discussed in terms of pressure drop per unit length, $\Delta p/\ell$, and friction factor, λ, according to the "European" definition, which leads to the basic relation

$$\lambda = \frac{\Delta p}{\ell} \frac{2d\rho A^2}{\dot{m}^2} \tag{1}$$

where d is the hydraulic diameter, A is the coolant cross section, ρ is the coolant density and $\dot{m}$ is the mass flow rate. The read-out of the axial pressure drop vs. water mass flow rate is plotted in Fig.3 for both "open channel", i.e. overall conductor, and "blocked channel", i.e. only bundle area. The test results are well fitted by a second order polynomial.

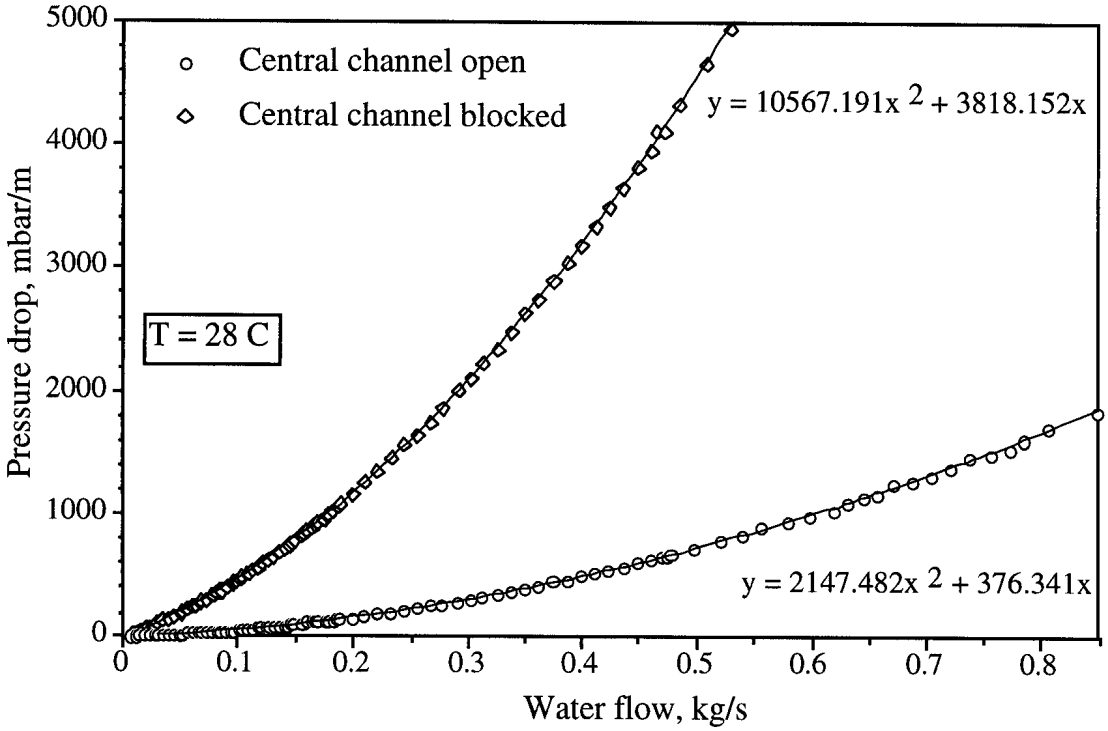

Figure 3. Axial pressure drop per unit length vs. water mass flow rate in the CS1 conductor with open and closed central channel

Assuming that the pressure is identical over a cross section in the bundle area and the central channel, the fraction of fluid flowing in the bundle area, α, can be found from the fitting curves of Fig. 3 as a function of the overall flow, x, imposing

$$10567.19(\alpha x)^2 + 3818.15\alpha x = 2147.48x^2 + 376.31x \qquad (2)$$

For $\dot{m}/\eta > 200$, i.e. over all the range of cryogenic operation, α is constant around 45%. From the flow partition, α, the ratio of the speed in the central hole, υ_H, to the speed in the strand bundle, υ_B, is

$$\frac{\upsilon_H}{\upsilon_B} = \frac{(1-\alpha)}{\alpha}\frac{A_{HeB}}{A_{HeH}} \approx 6.36$$

For the CSMC, with 7 g/s mass flow rate, we obtain υ_H = 36 cm/s and υ_B = 5.6 cm/s. The axial pressure drop of CS1 in operation can be scaled with the ratio $\dot{m}/\eta$ from the test results of Fig.3 and the data in Table 2, leading to $\Delta p/\ell$ = 0.79 mbar/m.

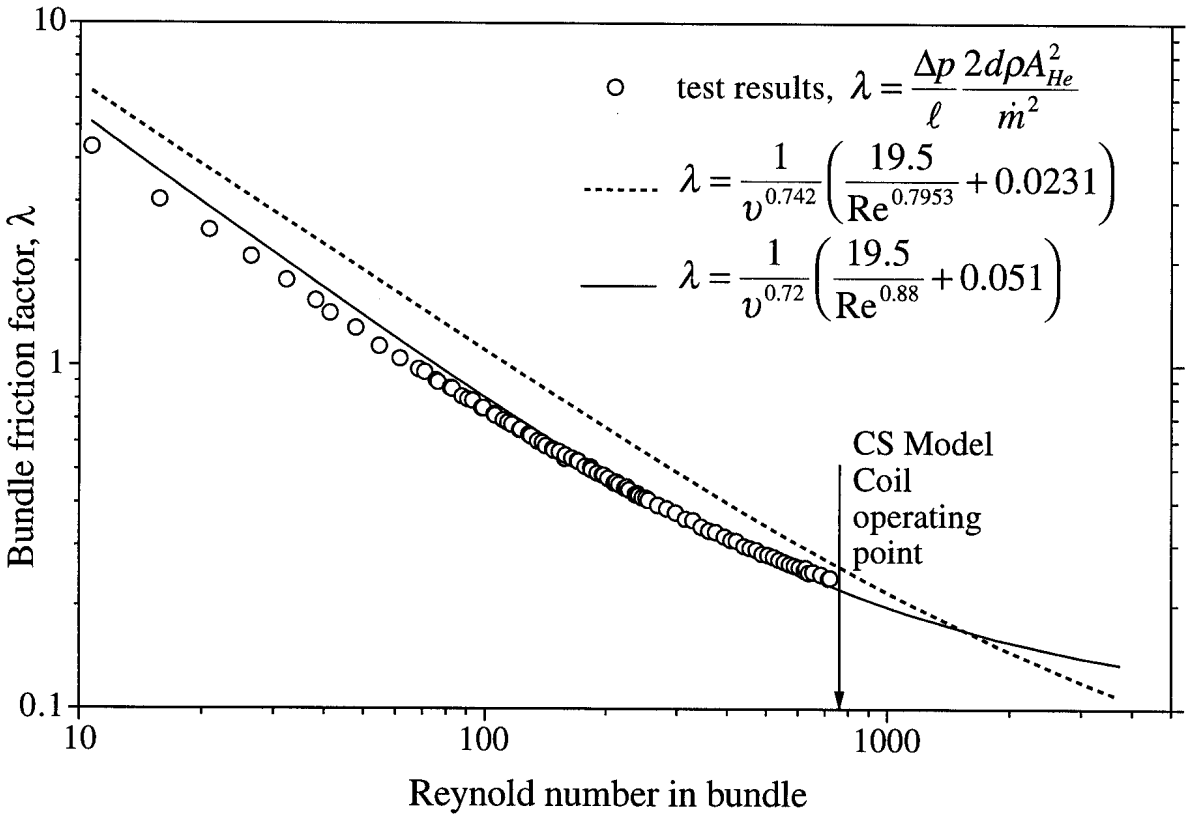

Figure 4. Friction factor in the strand bundle vs. Reynold number. The solid line is the general correlation proposed by Katheder [7]. The dotted line is from Nicollet [5]

The Reynold number in the bundle area, $\mathrm{Re}_B = \dot{m}_B d_B / A_{HeB}\eta$, can be assessed using the average hydraulic diameter in the bundle, d_B, and the Helium area, A_{HeB}, from Table 1. The friction factor, λ_B, in the bundle area, defined according to eq. (1) with index $_B$, and derived from the pressure drop results, $\Delta p_B/\ell$, is plotted in Fig.4 vs. the Reynold number: The solid line is the general correlation proposed by Katheder [7] on the basis of a broad range of experimental results on cable-in-conduit conductors. The dotted line is a correlation proposed by Nicollet [5] from pressure drop measurements carried out on an ITER conductor using Nitrogen at room temperature. The present

results for CS1 conductor are well matched by the general correlation proposed by Katheder, with only 5% deviation at the CSMC operating point.

From the flow partition α, it is possible to derive the friction factor in the central hole, λ_H

$$\lambda_H = \frac{\Delta p_{ov}}{\ell} \frac{2 d_{spi} \rho A_{HeH}^2}{((1-\alpha)\dot{m}_{ov})^2}$$

The results for the hole friction factor λ_H are plotted in Fig. 5 vs. the Reynod number in the central hole, $Re_H = (1-\alpha)\dot{m}_{ov} d_{spi} / A_{HeH} \eta$. The fitting curve $\lambda_H = 0.866\ Re^{-0.252}$ differs by a numeric factor from the Blasius correlation for turbulent flow in smooth pipes, $\lambda = 0.3164\ Re^{-0.25}$. The correction factor N = 0.866/0.3164 = 2.7 is due to the roughness of the spiral, which increases the turbulence compared with a smooth pipe. In the QUELL conductor, with similar geometry, the correction factor for the Blasius correlation was assessed in the range of N ≈ 2.5 [8].

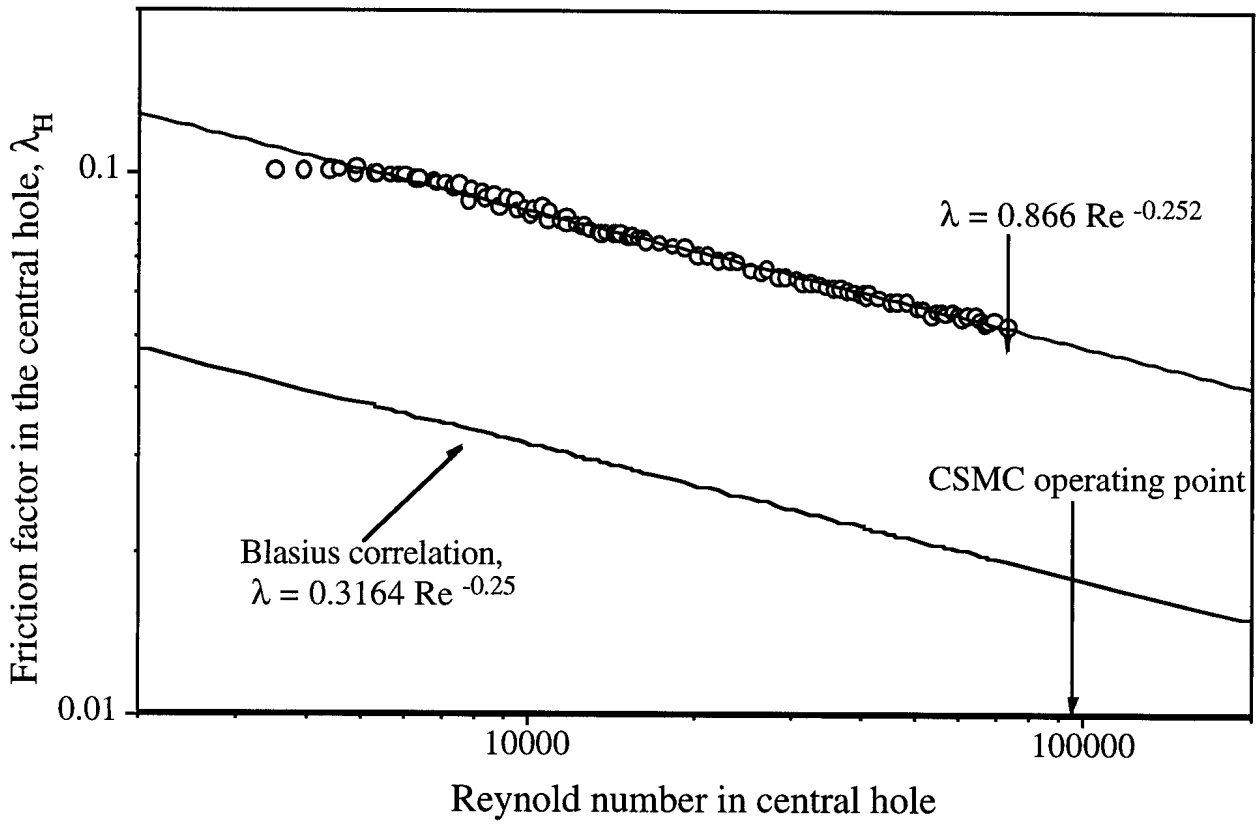

Figure 5. Friction factor vs. Reynold number for the central hole

The pressure drop at the radial inlet was measured both at the outlet (3 m away from the inlet, see Fig. 2) and by a sliding capillary tube as a function of the distance from the inlet. As the radial pressure drop is by far larger than the axial pressure drop over 3 m length, only a marginal difference, mostly buried in the error bar, is observed in the results as a function of the distance from the inlet. The pressure drop results are gathered in Fig. 6 vs. the mass flow rate. The solid and dotted lines correspond to the axial pressure drop, as measured in Fig. 3, multiplied by 50 and respectively 10. The pressure drop with the plain hole in the jacket is equivalent to about 50 m axial pressure drop in the conductor. With the machined steel shells, the pressure drop at the inlet decreases by a factor of five, corresponding to about 10 m axial pressure drop.

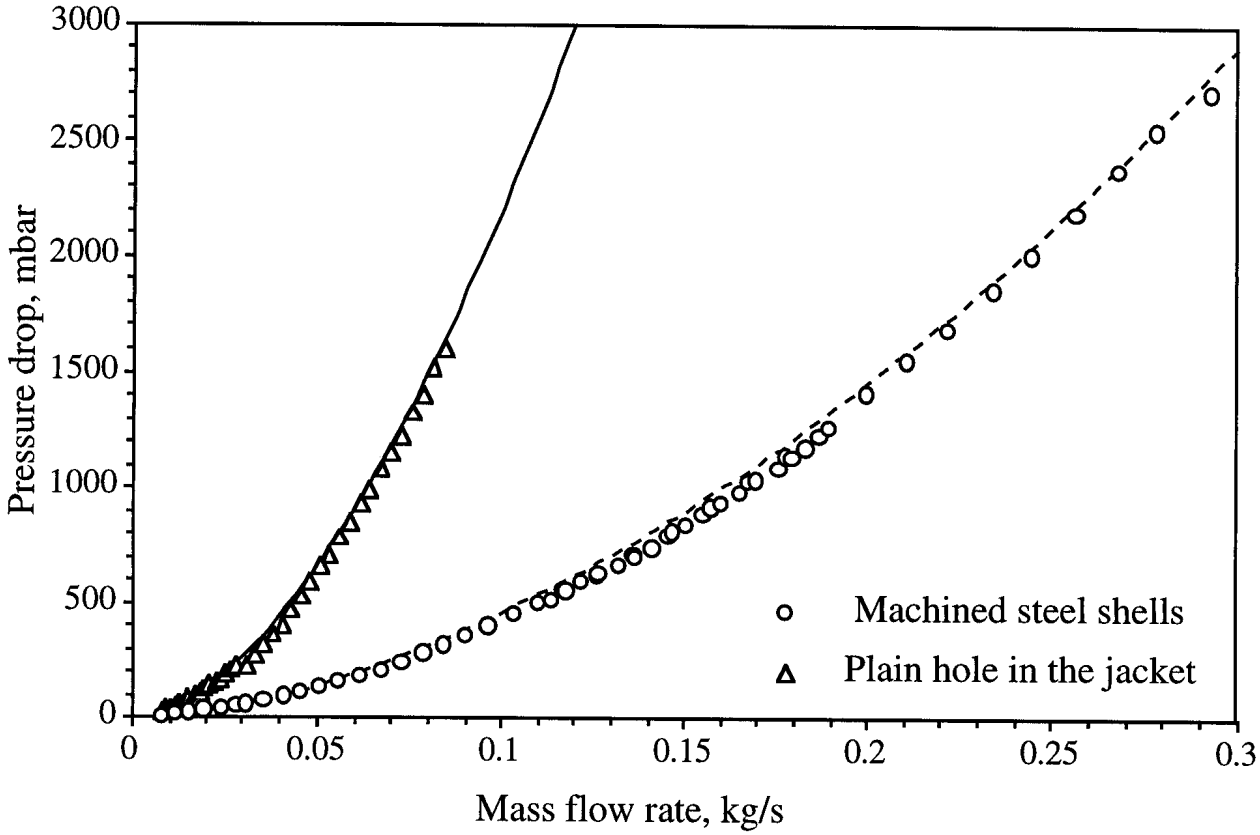

Figure 6. Radial pressure drop at the Helium inlet for plain hole (triangles) and machined shells (circles). The solid line is the axial pressure drop for 10 m conductor length, the dashed line for 50 m conductor length

4. Conclusion

The pressure drop measurements on the ITER conductor can be conveniently carried out using pressurized water at room temperature. The obtained Reynold numbers are close enough to the operating range of the CSMC.

The axial friction factor in the strand bundle can be satisfactorily fitted by the general correlation proposed by Katheder [7]. No new correlation is required. The axial friction factor in the central hole can be fitted by $0.866 \cdot Re^{-0.25}$, which is the Blasius correlation with a correction factor 2.7 for the spiral roughness.

The pressure drop per unit meter in the CSMC operating condition is predicted to be 0.79 mbar/m. Over a broad range of typical operating mass flow rate, 45% of the coolant flows in the strand bundle and the coolant speed in the central hole is 6.36 times higher than in the strand bundle. In the CSMC, the speed is predicted respectively 36 and 5.6 cm/s.

The pressure drop at the radial inlet can be reduced by a factor of 5 using machined steel shells instead of a plain hole in the jacket. The machined steel shells also provide a uniform cooling in the strand bundle, avoiding stagnant Helium regions. The pressure drop at the Helium inlet with machined shells is equivalent to 10 m conductor, i.e. has a marginal impact for hydraulic length >

100 m. The pressure drop with a plain hole in the jacket is equivalent to 50 m conductor, i.e. has a non-negligible impact on the overall pressure drop for hydraulic length of few hundreds meter.

Aknowledgement

The author is very indebted with Thomas Gloor for the pressure drop measurements. The technical support of the Paul Scherrer Institute is aknowledged.

References

[1] P. Bruzzone, N.Mitchell, M.Steeves, M.Spadoni, Y.Takahashi, V.Sytnikov, Conductor Fabrication for the ITER Model Coils, IEEE Mag 32, 2300 (1996)

[2] S. Nicollet, J.L. Duchateau, H. Fillunger, A. Martinez, S. Parodi, Dual channel cable-in-conduit conductors thermohydraulics: influence of some design parameters, IEEE Appl. Supercon. 10, 1102 (2000)

[3] ITER Personnel communication, CSMC QA documents, 1997

[4] P. Bruzzone, Fabrication of a Short Length of Wind-and-React Conductor, Final Report to the NET Team, Final Report Contract 88-745 A, ABB HIM 2042, May 1990

[5] S. Nicollet, H. Cloez, J.L. Duchateau, J.P. Serries, Hydraulics of the ITER toroidal field coil cable-in-conduit conductors, Proceedings of SOFT 98, 771

[6] H. Katheder, Reynold numbers for cable-in-conduit conductors, NET Internal Report, N7I70221/1/A, November 1992

[7] H. Katheder, Optimum thermohydraulic operation regime for cable-in-conduit superconductors, Cryogenics 34, ICEC Supplement, 595 (1994)

[8] K. Hamada et al., Thermal and hydraulic measurement in the ITER QUELL experiments, Adv. Cryog. Eng. 43, 197, 1998

Superconductors and Joints, Tests and Trends for Future Development

Pierluigi Bruzzone
CRPP-Technologie de la Fusion, 5232 Villigen-PSI, Switzerland

Abstract. The evolution of the fusion conductors is introduced with a review of few relevant milestones of the last 25 years. The cable-in-conduit conductors (CICC) are the most promising option for future fusion devices. The design aspects and test results of the ITER CICCs and joints in SULTAN are discussed with special attention to the interstrand resistance, current re-distribution, transient stability and hydraulic behavior. The challenges for future development are identified in the cost reduction and reliability issue.

1. Introduction

The subject of superconductors for fusion is old enough, at least 25 years, to have a history. However, the actual number of relevant realizations is in the range of a dozen and it is somehow questionable to draw clear, rational trend lines through a plot of scattered events. The conductor evolution is triggered by the *evolution of the operating requirement*, which runs parallel with the understanding of plasma engineering, the *improvement of the design*, which comes from the accumulation of the R&D results, and the *availability of advanced manufacturing technologies*. Despite the objective influence of the above constraints, the conductor appearance is sometimes affected by the personal taste of an individual engineer, who may put a kind of genetic imprint on "his" conductors.

2. A selection of milestones for fusion conductors

The toroidal field coils of the first ever superconducting fusion device, Tokamak-7, assembled about 1974-75 at the Kurchatov Institute (Moscow), are wound from a forced flow, monolithic conductor, see Fig. 1. Stability considerations moved the designers to prefer multiple cooling channels and pure copper matrix, obtained by electrolytic assembly [1], to the option of a soldered cable around a central pipe, developed in the same years at CERN-Brown Boveri [2]. The strands are not transposed in the strip conductor and the large induced current loops caused severe flux jumps, triggering quenches during ramp up and down. Nonetheless, the successful operation of the T-7 device triggered a large number of superconducting fusion machines in the following decade.

The toroidal field coils of the Tokamak-15 are the largest worldwide application of Nb_3Sn conductors, with over 11 tons of Nb_3Sn material (excluding stabilizer), compared to less than 9 tons in the recent ITER CSMC. In the react&wind conductor for T-15 [3], a flat cable is first heat-treated on a drum and then temporarily straightened to be bonded to two copper pipes by an electroplated Cu layer, see Fig. 1.

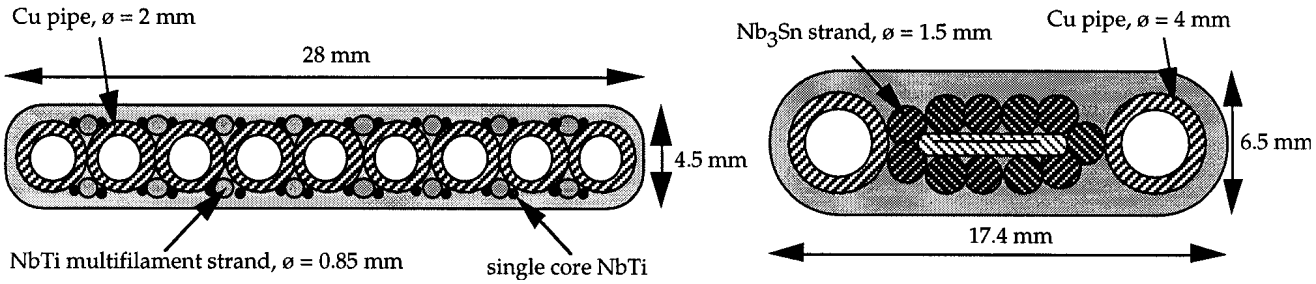

Fig. 1 Cross section of the forced flow conductor for T-7 (left) and T-15 (right)

Compared to T-7, the transposition problem is solved and the cooling channels, with larger diameter, are reduced to two. The conductor could withstand plasma disruption with field up to 40 T/s with minimum temperature rise, despite the large coupling currents loss. A steady state voltage was observed in some conductor sections, corresponding to an overall winding resistance in the range of 0.2 to 1 μΩ. After the T-7 and T-15 manufacturing experiences, the conductor assembly by electroplating was not applied anymore. The slow process speed, the large electric power requirement, the poor dimensional tolerance and large ac losses overcame the advantage of a low resistance matrix connecting the strands.

The toroidal windings of Tore Supra, assembled at Cadarache in 1987, still hold the flag of the largest mass, 160 tons, at a sub-cooled superfluid Helium bath, 1.8 K. The conductor [4] is a rectangular multifilament composite with mixed matrix of NbTi/Cu/CuNi, wound on the short edge to minimize the AC loss from the poloidal field variation. Compared to pool cooled conductors operating at 4.2 K, the copper cross section is small: for stability, the He bath enthalpy up to the λ point is available, due to the very high thermal conductivity of He II. The conductor is cryostable for mechanical and electromagnetic disturbances.

The two Japanese, superconducting fusion devices (TRIAM and LHD) have both pool cooled toroidal field coils. TRIAM [5] with a Nb_3Sn conductor operating at 6.2 kA, 11 T, is (and will remain for at least next ten years) the highest field operating fusion device. The helical windings of LHD, with a NbTi conductor at 13 kA and 6.9 T, hold the flag of the largest stored energy, 1 GJ, for a pool cooled magnet. The three constraints for conductor evolution should have produced, for TRIAM and LHD, two substantially different conductor layouts: higher field vs. lower field, Nb_3Sn vs. NbTi, D-shaped vs. helical windings and over ten years of R&D progress and technology improvement. However, looking at Fig. 2, it's evident from the first glance how strong the genetic imprint of the manufacturer (Hitachi Cable) has driven the conductor layout. Both conductors, and before them the JA-LCT conductor in 1979 [6], have the current carrying elements soldered with an Al stabilizer into a U-shaped copper casing, with surface treated for enhanced heat exchange. The technology improvements, e.g. the electron beam welding of the copper casing and the CuNi cladding of the pure Al stabilizer in the LHD conductor [7], affect only marginally the designer approach. The three Hitachi conductors in Fig. 2 were designed to be cryostable. However, transient instability has been observed in the LHD winding [8] below the expected "cold-end" recovery current. Despite the successful performance of the above pool cooled fusion windings, the requirement for higher field and volume in the future fusion machines penalizes the pool cooling option. The main reasons are the need to withstand high loads in the winding (hardly met by a Helium transparent conductor stack) and the high voltage exposing, under upset operating conditions, to the risk of a short through gas bubbles in the coolant (Paschen minimum discharge).

The WH-LCT [6] is another milestone for fusion conductors, as first large magnet wound from a cable-in-conductor conductor (CICC) in 1981. The bundle of non-coated, Nb_3Sn strands, encased in a Ni alloy sheath, see Fig. 3, is wound according to the react&wind method. Large, local voltages were detected at several sections of the winding. Such degradation led to an overall resistance in excess of 1.2

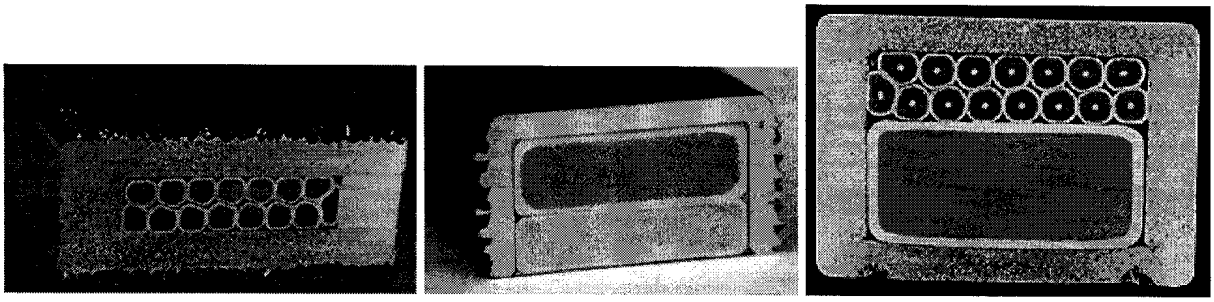

Fig. 2 Three pool cooled conductor generations from the same (Hitachi) family: from left, the JA-LCT NbTi conductor (≈1979), the Nb_3Sn Al stabilized conductor of TRIAM (≈ 1984) and the helical coil LHD NbTi, Al stabilized conductor (≈1995))

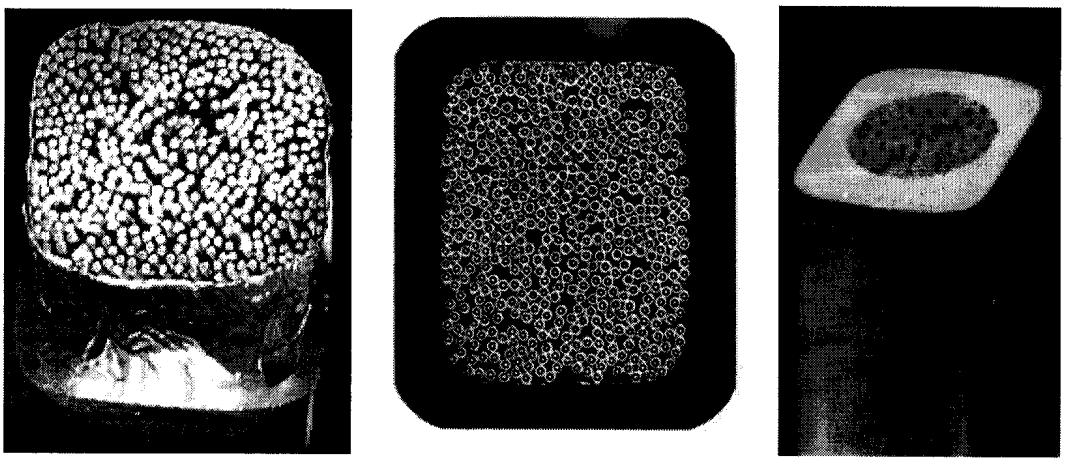

Fig. 3 Three milestones of cable-in-conduit conductors. From left to right, the Nb_3Sn WH-LCT, the LHD poloidal coil conductor and the W7-X with Aluminum alloy jacket

μΩ at the rated current of 17.7 kA. Despite the partly disappointing performance of the WH-LCT, the CICC became more and more popular in the fusion magnets community of the last 15 years, not only for prototype coils (e.g. the Demo Poloidal Coil project at Naka, Polo at Karlsruhe and the ITER model coils) but also for fusion devices: the poloidal coils of the LHD, the W7-X magnet system, K-Star, HT-7U.

3. Design issues and test results for the large ITER CICCs

The above achievements set milestones for superconducting fusion magnets. However, the designers do not learn much from the coil operation. The effectiveness of the conductor layout and its margin can seldom be verified in an operating device: either the mechanical load or the cooling plant hardly allows achieving the dc limit in a coil. The ac losses cannot be separated from other thermal loads and the stability cannot be quantified due to the lack of suitable, controlled transient disturbances. In a full size, short length conductor test, the design verification can be pushed to the limit and intrusive instrumentation (not allowed in a coil) can be placed anywhere. The large conductor test facility SULTAN [9] at CRPP-Villigen acted in the last ten years as a unique feedback tool for conductor design. With a large experimental volume at 11 T, a current source up to 100 kA, supercritical Helium over a broad temperature range and superimposed transverse pulsed field up to 2 T and dB/dt in excess of 50 T/s, a full characterization of the ITER conductors and joints has been carried out, exploring operating conditions crucial for the design but practically prohibited in a coil test. Ten Nb_3Sn and NbTi ITER-related full size conductors and joints, manufactured in Japan, Europe and US, have been tested in SULTAN from 1996 to 1999.

3.1 Strand coating and interstrand current sharing

One of the most attractive features of the CICC is the possibility to maintain low ac losses for large conductor size, what is just impossible for monolithic or soldered conductors. To control the ac losses in a CICC, resistive barriers must be inserted between the current carrying elements to prevent large induced current loops. The plain solution of an insulating varnish at the strand surface proved to be unsuccessful in the DPC-U coil, which suffered severe instability [10], due to the inability to re-distribute the current among the strands after a fast ramp. In the Polo conductor [11], see Fig. 4, the subcables were also separated by insulating wraps and the ac losses were extremely low (only hysteresis loss). A careful control of the transposition (two-stage cable around a central pipe) and a consistent layout of the joints (subcables connected one by one) produced an acceptable current balance: the dc performance was reduced "only" to 70% of the expected critical current and the stability was excellent. The option "no coating", i.e. bare copper surface, has been used at Toshiba for the Nb_3Sn DPC-TJ conductor [12], the NbTi poloidal field coils of LHD [13], as well as for a NbTi prototype

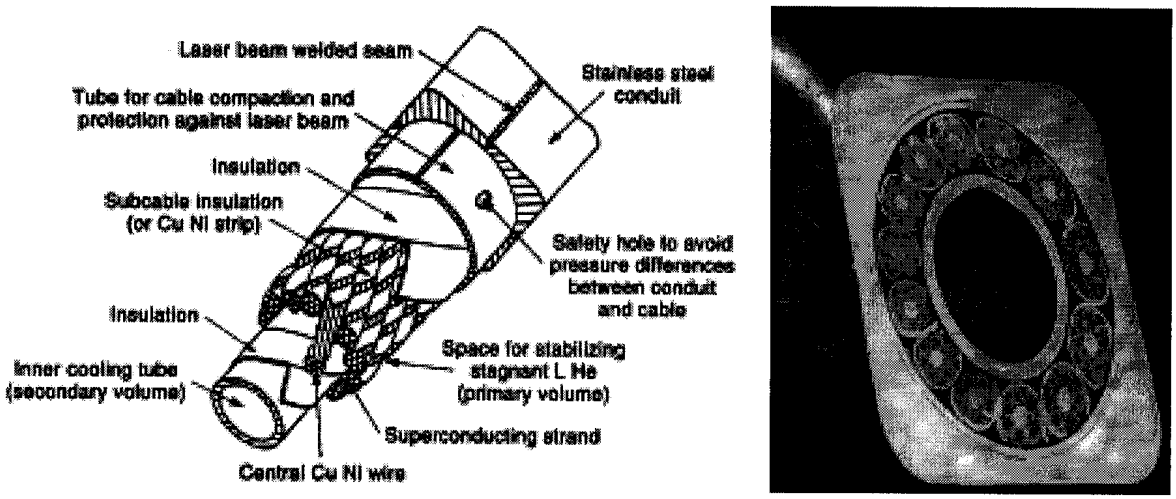

Fig. 4 The Polo conductor, with two separate Helium chambers

SMES coil [14]. In the three cases, the coupling loss in operation was high and multiple time constants were observed, with average value far above 1 second, i.e. unacceptable for pulsed operation.

For Nb_3Sn CICCs, the preferred strand coating is an electroplated Cr layer, which prevents solid state interdiffusion at the strand crossovers during the conductor heat treatment (sintering). Early coupling loss measurements on short length, Cr plated CICCs reported large time constant, in the range of hundreds ms [15], in contrast with coil results [12]. The contradiction was solved after observing that the interstrand resistance in the Cr plated, heat treated bundle is a function of the cyclic transverse load and increases up to 0.5 - 1 $\mu\Omega$·m [16]. The electromagnetic load in operation releases the mechanical engagement at the strand crossovers and restores the high interstrand resistance, with coupling loss time constant in the range of few ms. In SULTAN, the coupling currents loss has been measured by gas flow calorimetry with superimposed ac and dc field and dc transport current. Table 1 summarizes the very low loss results, with $n\tau \leq 5$ ms, obtained for the ITER Model Coils conductor samples [17, 18, 19]. The conservatism of the design criteria, with assumed coupling loss $n\tau = 150$ ms, can be now removed based on the experimental results, with substantial impact on the heat load balance and operating temperature.

After stating that the contact resistance of the Cr plating is large enough to cut the interstrand coupling loss, the question arises if it is also low enough to allow current re-distribution among the strands. When the CICC dc performance is satisfactory, i.e. scalable to the strand data, this is evidence that the current re-distribution occurs and the interstrand resistance is low enough, as it was verified in the SeCRETS experiment in SULTAN [20]. At interstrand resistance higher than 1 $\mu\Omega$·m, e.g. when the subcables are wrapped by high resistivity strips, the interstrand current sharing is hampered and a degradation of the dc performance may be observed in case of unbalanced current distribution. Evidence was shown in the short sample CS1 test in SULTAN, where an artificially unbalanced current distribution was created by chopping the hairpin joint, see Fig. 5 [17].

Table 1
Coupling loss constant, $n\tau$, measured on ITER conductors by gas flow calorimetry in SULTAN

Conductor sample	*$n\tau$ result, ms*	*Reference*
ITER - CSMC-CS1	3.1 @ 2 T	[17]
ITER - CSMC-CS2	2.4 @ 4 T	[19]
ITER - TFMC	5.4 @ 2 T	[18]

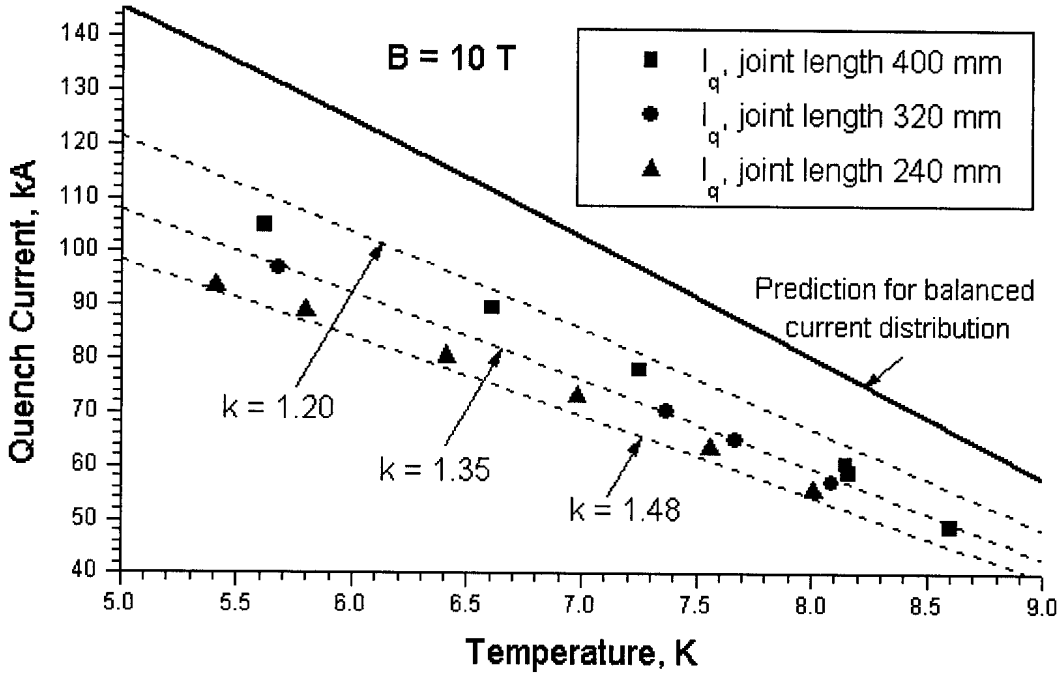

Fig. 5 DC performance degradation measured in SULTAN on the CS1 ITER conductor, with artificially induced current unbalance by chopping the hairpin joint and high resistivity subcable wraps. The correction factor k is drawn from a model [17]

3.2 Transient Stability

At plasma disruption, large field transients affect the ITER CICCs, with energy deposition by ac losses on the time scale of few hundreds milliseconds. In the design criteria, large (expensive) temperature margins are foreseen to prevent a conductor quench at plasma disruption. The strength of the transient field induced by the ITER plasma disruption can be conveniently expressed by $\int \dot{B}_{\perp}^2 dt \approx 0.5\ T/s^2$. In SULTAN, plasma disruption can be effectively simulated up to several tens T/s^2 by a set of pulsed field coils, which generate a transverse field, superimposed to the background field, of variable amplitude and 110 ms duration. The actual temperature margin necessary to withstand a field transient of variable amplitude has been measured on a section of ITER conductor in SULTAN, see Fig.6. The results show that a small temperature margin, less than 0.5 K, is sufficient to withstand field transient by far larger than the plasma disruption. The feedback of the stability results on the design criteria allows to reduce the temperature margin allocated for plasma disruption, with substantial resizing of the superconductor cross section.

3.3 Multiple channels, pressure drop, coolant speed

The CICCs are frequently advertised for the superior stability, due to the large wet perimeter and small hydraulic diameter in the strand bundle. However, the large fanning friction factor, turns into a large pressure drop per meter and a drastic limitation of the mass flow rate for long conductor sections. In case of quench, the peak pressure of the heated Helium may be even dangerous for the coil integrity. A pressure release channel is included in several CICC design to mitigate the quench pressure rise, see Fig. 7. In the channels with larger hydraulic diameter, the coolant speed, υ_{hole}, is large and the average residence time of the coolant in the winding is shortened. However, the reduced coolant speed in the strand bundle, υ_B, ($\upsilon_{hole}/\upsilon_B > 6$ in the ITER conductor [21]) has a negative impact on the stability [20],

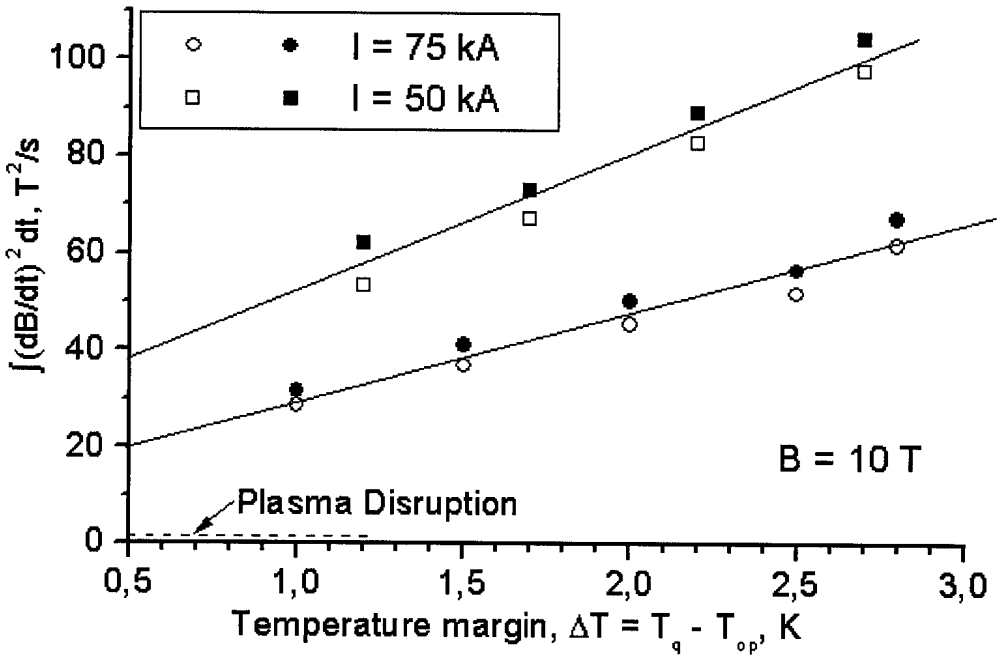

Fig. 6 Stability under transverse pulse field vs. temperature margin for the ITER CS1 conductor. The full symbols show a quench. The field transient of the plasma disruption can be withstood with minimum temperature margin.

as the steady state heat exchange coefficient, h_{ss}, increases with the coolant speed according to the Dittus-Bölter correlation, $h_{ss} \propto v^{0.8}$.

If the advantages of the high coolant speed in the bundle are disregarded, the design approach of the Polo conductor [11] sounds extremely clever, Fig. 4. The bundle region contains stagnant, pressurized supercritical Helium and exchanges heat by conduction to a large central channel containing high speed two-phase Helium. Opposite to the cooling by forced supercritical Helium, the conductor temperature is constant over the winding and the Helium expansion in the bundle, e.g. during a pulse, does not choke the central channel. However, the complexity of the cryogenic system for Polo (including joints and feeders) should not be underestimated.

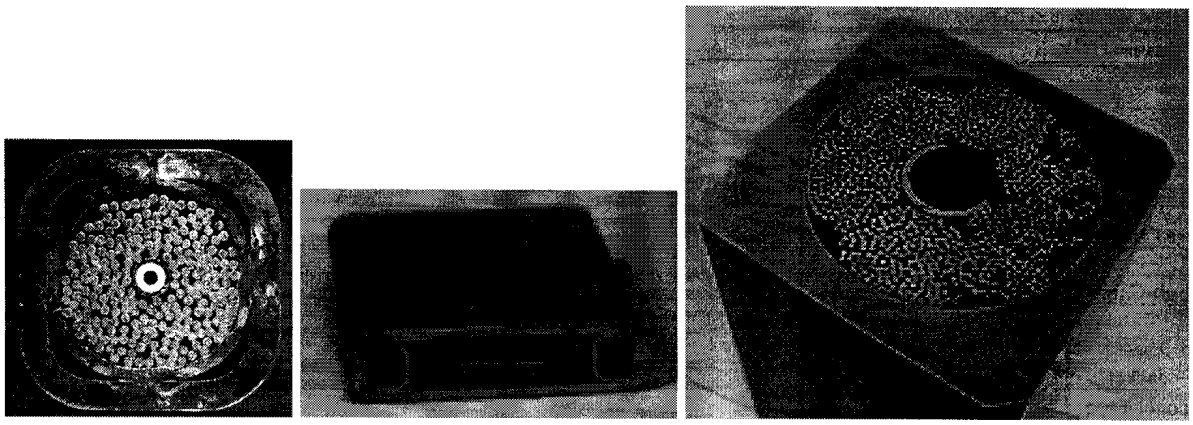

Fig. 7 Three Nb_3Sn CICCs with pressure release channels at the four corners (US-DPC, right), at both sides (DPC-EX, middle) and at the center (ITER-CSMC, left)

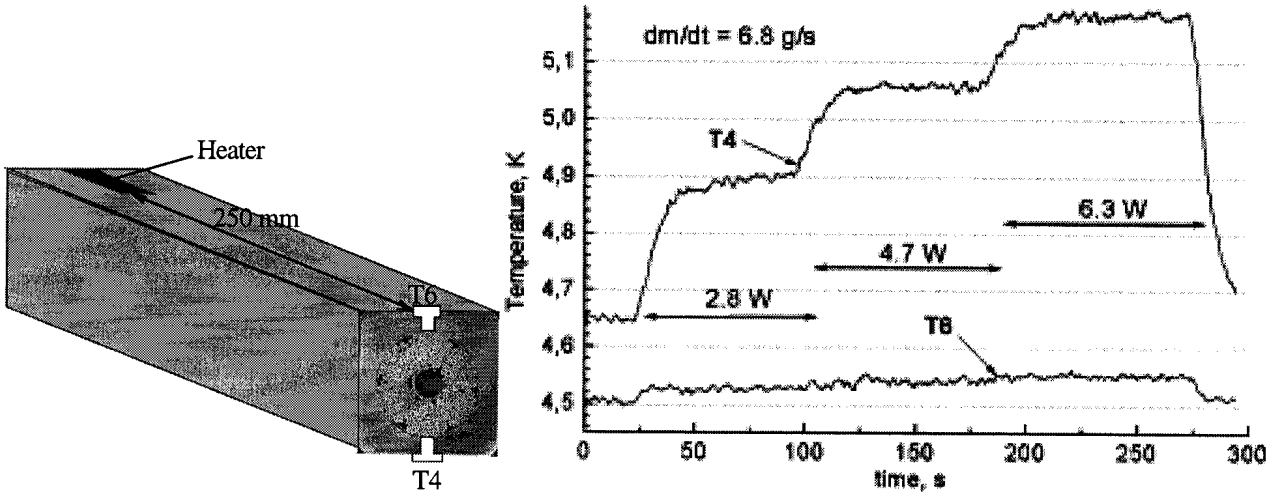

Fig. 8 Temperature gradient over the cross section of the ITER-CS1 conductor. Switching the heater on one side of the jacket to three power levels, a steady state temperature difference builds up between the opposite faces (T4 and T6 sensors) and is maintained over a long length due to the poor radial mass exchange

A major drawback of large CICCs with pressure release channel is the non-isothermal cross section. Whenever a partition of the cable space is done, e.g. by wraps, spiral or perforated pipes, the radial mass exchange, which is only driven by sensible pressure differences, drops dramatically. It was verified during the ITER-CS1 test in SULTAN, see Fig. 8 [17], that temperature differences as large as 0.5 K may persist in adjacent sections of the strand bundle due to the lack of radial mass exchange caused by the subcable wraps. This result, together with the dc current re-distribution finding of Fig.5 and the coupling loss result, suggests that overall beneficial effects can be obtained removing the subcable wraps from the ITER cable.

4. The joints for large cable-in-conduit conductors

The joints vary in size, geometry, complexity and performance, but there is no convergence among the possible options. The Helium tightness is the prime, mandatory requirement. However, the perception of the leak risk is quite different among the designers, some of them accepting very aggressive metal joining techniques, which can hardly be repaired in case of failure.

A low dc resistance is always welcome at the joint, but it's hard to set a threshold for actual rejection. The dc target for joints can be formulated either as temperature increase, power or resistance criterion [22]. Table 2 summarizes the dc performance and the geometry of joints for fusion CICC. A butt weld (resistance weld) was successfully used in the WH-LCT, but proved to be not satisfactory for the large ITER-CS conductor, where eventually a diffusion bonded butt joint was adopted in the outer module. For the lap and hairpin geometry, a broad range of resistance values can be achieved, depending on void fraction, contacting methods, etc. In most, non-soldered connection, the reproducibility of the performance is an issue. For the ITER joints, after several iterations the resistance requirement could be fulfilled by all the joint layouts, see Table 2.

As the joints are mostly placed at low field, much larger ac losses can be tolerated, compared with the plain, high field conductor. Large joint ac losses may lead to a quench only at fast pulse rate, as it was the case for the solder filled lap joint of the US-DPC [35], despite the separate cooling by He bath [36]. In the Polo coil [11], the subcable separation was maintained at the joint and the envelope of the subcable lapjoints was encircled by a thick Cu cylinder to shield the ac field. For the ITER hairpin joints measured in SULTAN, the ac losses are dominated by the eddy currents loss in the large copper blocks [18, 19]. However, one order of magnitude smaller loss are obtained by a low resistance, soldered joint developed at CRPP [24], with segmented copper blocks.

Table 2

. Summary of dc performance for fusion cable-in-conduit joints

CICC	*Joint Resistance*	*Operating Field*	*Joint geometry*
WH-LCT, Nb_3Sn	≈ 1 nΩ	3 T, 17 kA	Butt welded
DPC-TJ, Nb_3Sn	> 3.5 nΩ	1.4 T, 24 kA	Solder filled overlap
US-DPC, Nb_3Sn	< 0.5 nΩ	2.2 T, 30 kA	Solder filled overlap
LHD-Poloidal, NbTi	0.14 nΩ	3.6 T , 20 kA	Filament joining
Polo, NbTi	6 nΩ	2 T, 15 kA	Split subcable soldered overlap
W7-X, NbTi	0.5 nΩ	6 T, 17 kA	Soldered Overlap
ITER-CSMC outer	3.2 nΩ	2.6 T, 50 kA	Diffusion bonded butt
ITER-CSMC inner	2.2 nΩ	4 T, 50 kA	Overlap joint, pressure contact
ITER-Nb_3Sn insert	3.1 nΩ	4.5 T, 50 kA	Overlap joint, pressure contact
ITER-Nb_3Al insert	3.5 nΩ	4.5 T, 50 kA	Overlap joint, pressure contact
ITER - TFMC	2.2 nΩ	5 T, 50 kA	Overlap joint, pressure contact
ITER - CRPP improv.	1.3 nΩ	5 T, 50 kA	Overlap joint, soldered surface

In CICC with large transverse resistance, the current distribution may be affected by the distribution of the strand-to-termination conductance [17]. In the termination of a large CICC it is virtually impossible to obtain that each strand has the same number of contacts to the feeder. On the other hand, the distribution of strand-to-termination conductance is mostly controlled by the interstrand resistance at the termination and is much more balanced in comparison with the distribution of strand-to-feeder contacts [25]. A balanced resistance distribution at the joint is welcome, but should not become a strict requirement. As long as the interstrand resistance in the CICC is low enough to allow interstrand current sharing, see section 3.1, the current distribution can easily re-adjust .

5. Challenges for development of fusion conductors and joints

Almost all the fusion conductors of the last 25 years substantially fulfilled the operating requirement. No serious failure has been reported although sometime the actual operating limit did not correspond to the design value. The performance of the ITER conductors developed for the model coils can be judged satisfactory, but there is still room for improvement. A mandatory requirement for an effective R&D work is that only *full-size* conductor and joints are used and the test range must not be limited to the "acceptance" threshold, but has always to be pushed to the limit.

The actual challenge for the future of the fusion conductors is to *reduce the cost.* Opposite to other applications (e.g. accelerator magnets), fusion will have to compete on the market with other energy sources: the superconductors are now a major cost item in a fusion plant and a reduction of the conductor cost is an important goal. A big potential for cost reduction is the refinement of the design: the margin allocation must be continuously updated according to the verification test on full size conductors. The strong pressure for the successful demonstration of a prototype pushes the designers to be very conservative and use generous margins. However, most of the margins act as a cost multiplicators. A conductor with 2 K temperature margin is not necessarily better than one with 1 K margin (even if the designer may sleep better with it), but it's definitely more expensive.

Other ways to reduce the conductor cost are linked to the manufacturing processes. For example, the market price of a Nb_3Sn composite is independent on its copper fraction. A substantial cost reduction can be achieved segregating the copper as separate wire and reducing the weight of the Nb_3Sn composite by maintaining the original superconductor cross section, with marginal compromises on transient stability, as it was demonstrated in the SeCRETS experiment in SULTAN [20]. The jacketing options, as well as the jacket design, may need to be revised giving higher priority to the cost issue. The

successful demonstration of very sophisticated jacketing/encasing techniques (DPC-TJ [26], Polo [11], ITER-TFMC [27]) is not a sufficient reason to apply it in the future, as long as the process cost is not competitive. Not only the cost, but mostly the price of the conductor must be reduced by a fair competition among industrial suppliers and open, "non-protected" bidding actions.

The other big challenge for fusion conductor and joints is the *reliability and manufacturing risk*. As a part of the superconducting magnet system, the conductor and the joints must be conceived as a utility with the same reliability degree of a transformer or a generator. Complexity is seldom an adequate cure for technical problems and reparability is not an alternative to reliability. For example, excellent results could be obtained for dc and ac behavior in an improved joint developed at CRPP [24] using basic technology and low risk process. Professional methods for reliability assessment, e.g. probabilistic analysis, should be part of the design. The selection of the manufacturing procedure should also be done in terms of applicable QA methods and risk assessment.

6. Conclusion

The test in SULTAN of full size ITER conductors allows extending the range of characterization well beyond the possibilities of a coil test. The most relevant results include: low coupling loss ($n\tau \leq 5$ ms) under actual operating conditions, excellent stability under transverse field pulse, thermal gradients and hampered current re-distribution due to the high resistivity subcable wraps. A feedback to the design criteria will allow reducing the level of conservatism.

The ITER joints have different layouts. All of them fulfil the resistance requirement, but they differ substantially for the complexity and associated manufacturing risk. The ac losses performance is also different, with large losses in the joints using large copper blocks.

The cost reduction and the reliability issue are the challenges for future development and must receive the same attention in the conductor and joint design as the performance excellence.

References

[1] V. N. Agureev, V. E. Keilin, E. Yu. Klimenko, B. N. Samoilov, Electroplated stabilized multifilament superconductor, IEEE Trans. Magn. 11, 303 (1975)

[2] M. Morpurgo, The design of the superconducting magnet for the "OMEGA" project, Particle Accelerators 1, 255 (1970)

[3] E. Yu. Klimenko et al., Superconducting conductor for T-15 toroidal magnet, Soviet Atomic Energy (a translation of Atomnaya Energiya) 63, 756 (1987)

[4] B. Turck, K.J. Best, Hoang Gia Ky, Fabrication and test results of the conductor for the toroidal field coils of tore supra, Fusion Technology 1986 (Proc. of SOFT 14), 1675

[5] Y. Nakamura, A. Nagao, N. Hiraki and S. Itoh, Reliable and stable operation of the high field superconducting tokamak TRIAM-1M, Proceedings of Magnet Technology Conference MT-11, 767 Tsukuba, 1990 (Elsevier).

[6] The IEA Large Coil Task, Fusion Engineering and Design, 7, 1&2, 1988

[7] N. Yanagi et al., Development, fabrication, testing and joints of Aluminum stabilized superconductor for the helical coils of LHD, Proc. of ICEC16/ICMC, Kitakyushu, 751, 1996 (Elsevier)

[8] N. Yanagi et al., Analysis of normal transition event of the LHD helical coils, IEEE Appl. Supercon. 10, 610 (2000)

[9] A. M. Fuchs et al., Facility status and results on ITER full-size conductor tests in SULTAN, To be published in IEEE Appl. Supercon 11

[10] Y. Takahashi, N. Koizumi, Y. Wadayama, K. Okuno, M. Nishi, T. Isono, K. Yoshida, M. Sugimoto, T. Kato, T. Sasaki, F. Hosono, T. Ando, H. Tsuji, Experimental results of stability and current sharing of NbTi cable-in-conduit conductors for the poloidal field coils, IEEE Appl Supercon, 3, pp. 610-613, 1993.

[11] M. Darweschsad et al., development and test of the poloidal field prototype coil POLO at the Forschungszentrum Karlsruhe, Fusion Engineering and Design 36, 227 (1997)

[12] K. Okuno et al., AC loss performance of 1 m bore, large-current Nb_3Sn superconducting coils in JAERI demo poloidal coil project, IEEE Trans. Appl. Supercond. 3, 602 (1993)

[13] K. Takahata et al., Stability tests of the NbTi cable-in-conduit superconductor with bare strands for demonstration of the large helical device poloidal field coils, *IEEE Trans. Magn.* **30**, 1705 (1994)

[14] T. Hamajima et al., AC loss performance of the 100 kWh SMES model coil, IEEE Appl. Supercon. 10, 812 (2000)

[15] A. Nijhuis, H.H.J. ten Kate, P. Bruzzone, L.Bottura, Parametric Study on Coupling Loss in Subsize ITER Nb3Sn Cabled SpecimenIEEE Mag 32, 2743 (1996)

[16] A. Nijhuis, N. H. W. Noordman, H.H.J. ten Kate, N. Mitchell, P. Bruzzone, Electromagnetic and mechanical characterization of ITER CS-MC Conductors affected by transverse cyclic loading, part 2: Interstrand resistance, IEEE ASC 9, 754 (1999)

[17] P. Bruzzone, A.M. Fuchs, G. Vecsey, E. Zapretilina, Test Results for the high field Conductor of the ITER Central Solenoid Model Coil, Adv. Cryog. Eng., 45, 729-736 (2000)

[18] D. Ciazynski, J-L. Duchateau, T. Schild, A.M. Fuchs, Test results and analysis of two European full size conductor samples for ITER, IEEE Appl. Supercon. 10, 1058 (2000)

[19] Ph. Michael, USP conductor pulse field measurements, Presented at Workshop on SULTAN test results, Villigen June 22-24 1999

[20] P. Bruzzone et al., Test results of SeCRETS, a stability experiment about segregated copper in cable-in-conduit conductors, To be published in IEEE Appl. Supercon 11

[21] P. Bruzzone, Pressure drop and Helium inlet in ITER CS1 conductor, Paper F-35 at this conference

[22] P. Bruzzone, N. Mitchell, D. Ciazynski, Y. Takahashi, B. Smith, M. Zhelamskij, Design and R&D Results of the Joints for the ITER Conductor, IEEE Appl Supercon 7, 461 (1997)

[23] M. M. Steeves et al., The US demonstration poloidal coil, IEEE Mag 27, 2369 (1991)

[24] P. Bruzzone, Manufacture and Performance results of an improved joint for the ITER Conductor, Adv. Cryog. Eng., 45, 737- 744 (2000)

[25] P. Bruzzone, Contact resistance distribution at the terminations of cable-in-conduit conductors, To be published in IEEE Appl. Supercon 11

[26] M. Nishi, T. Ando, H. Tsuji, H. Mukai, T. Hamajima, T. Fujioka, Development of high current density, large superconducting coil for fusion machines: the DPC-TJ program, Cryogenics, 33, 573 (1993)

[27] R. Maix et al., Manufacture, assembly and QA of the ITER toroidal field model coil, IEEE Appl. Supercon. 10, 584 (2000)